Experimental Realization of a Protected Superconducting Circuit Derived from the 0–π Qubit

András Gyenis[1,†] Pranav S. Mundada[1,†] Agustin Di Paolo[2,†] Thomas M. Hazard[1]
Xinyuan You[3] David I. Schuster[4] Jens Koch[5] Alexandre Blais[2,6] and Andrew A. Houck[1,*]

[1]*Department of Electrical Engineering, Princeton University, Princeton, New Jersey 08544, USA*

[2]*Institut quantique & Département de Physique, Université de Sherbrooke, Sherbrooke, Quebec J1K 2R1, Canada*

[3]*Graduate Program in Applied Physics, Northwestern University, Evanston, Illinois 60208, USA*

[4]*The James Franck Institute and Department of Physics, University of Chicago, Chicago, Illinois 60637, USA*

[5]*Department of Physics and Astronomy, Northwestern University, Evanston, Illinois 60208, USA*

[6]*Canadian Institute for Advanced Research, Toronto, Ontario M5G 1M1, Canada*

Encoding a qubit in logical quantum states with wave functions characterized by disjoint support and robust energies can offer simultaneous protection against relaxation and pure dephasing. One of the most promising candidates for such a fully protected superconducting qubit is the 0–π circuit [Brooks *et al.*, Phys. Rev. A **87**, 052306 (2013)]. Here we realize the proposed circuit topology in an experimentally obtainable parameter regime, where the ground-state degeneracy is lifted but the qubit is still largely noise protected. More precisely, the logical states of this qubit feature disjoint support and are exponentially protected against relaxation and exponentially (first order) protected against dephasing due to charge (flux) noise. We name the resultant device the "soft 0–π qubit." Multitone spectroscopy measurements reveal the energy-level structure of the system, which can be precisely described by a simple two-mode Hamiltonian. Using a Raman-type protocol, we exploit a higher-lying charge-insensitive energy level of the device to realize coherent population transfer and logical operations. The measured relaxation ($T_1 = 1.6$ ms) and dephasing ($T_R = 9$ μs, $T_{2E} = 25$ μs) times demonstrate that the soft 0–π circuit not only broadens the family of superconducting qubits but also constitutes an important step toward quantum computing with intrinsically protected superconducting qubits.

I. INTRODUCTION

Preserving the coherence of quantum superpositions over prolonged times is key for large-scale quantum-information processing [1–3]. Besides implementing quantum error correction schemes [4–7], a complementary approach to conserve the coherence of a superconducting qubit is to develop circuits that are intrinsically protected against decoherence [8–13]. Such protection arises because quantum information is encoded in delocalized collective states capable of withstanding errors originating from local noise in these circuits [14–16].

However, intrinsically protected circuits generally impose taxing requirements on the parameters of the physical device [17–21] that are beyond the feasibility of current superconductor-based technologies. Thus, finding a balance between the degree of protection and the viability of experimental realization of the circuit is essential.

Noise-protected qubits are required to be robust with regard to both energy relaxation and pure dephasing processes. According to Fermi's golden rule, the decay rate of the excited state of a qubit is linked to the matrix element of the qubit states via a noise operator. Thus, states that are *localized* in disjoint regions of the configuration space can reduce the rate of energy relaxation [10,13,22–25]. We describe such a scenario with the term "wave functions with disjoint support," where the support of a wave function refers to the space where the probability amplitude is not exponentially suppressed. In contrast, systems that are protected against pure dephasing due to charge (flux) noise feature qubit wave functions that are *delocalized* over the

eigenstates of the charge (flux) operator. For example, the charge-noise insensitivity of the transmon qubit [26] arises from wave functions that are delocalized in charge space; similarly, the flux-insensitive parameter regime of the fluxonium qubit is characterized by delocalized wave functions in phase space [27]. Consequently, simultaneous protection against energy relaxation and pure dephasing imposes competing constraints on qubits with a single degree of freedom and ultimately can lead to intrinsic limitations on the coherence times. Unlike single-mode qubits, such as the transmon, superconducting circuits with more degrees of freedom featuring wave functions in a multidimensional configuration space can be simultaneously protected against energy relaxation and pure dephasing. One such example is the intrinsic protection of the two-mode 0–π qubit [11,12], where the combination of one delocalized flux mode (light-fluxonium-like) and one delocalized charge mode (transmonlike) supports the realization of states that are characterized by disjoint support as well as charge insensitivity and flux insensitivity. In this work, we realize a slightly modified version of the 0–π qubit [11,12,17–19] by reducing the energy scales of its parameters to an experimentally obtainable regime. We demonstrate exponential protection against relaxation for the offset-charge-insensitive logical states and show that dephasing due to flux noise is suppressed to first order. The performance of the device is still affected by the photon shot noise [28] intrinsically arising from the presence of a harmonic mode in the circuit. Finally, we also note that due to the "softened" parameter regime of the device, the qubit energy is nondegenerate, and thus coherent operation relies on higher lying energy levels.

This paper is organized as follows. In Sec. II, we introduce the *soft* 0–π circuit with the attainable energy scales. In Sec. III, we present the fabricated device and the spectroscopy measurements to demonstrate the energy structure of the qubit as a function of external charge and flux variables. To map the logical qubit states, we demonstrate Autler-Townes spectroscopy in Sec. IV. We use Raman gates to perform logical operations between the qubit states, which is described in Sec. V. Finally, we discuss the current challenges and theoretically estimate the possible dephasing mechanisms limiting the performance of our qubit in Sec. VI. We provide details about the fabrication, numerical calculations, modeling, and the motivation for the parameter choice in the appendixes.

II. THE SOFT 0–π QUBIT

In this section, we first introduce the general features of the 0–π circuit proposed by Brooks *et al.* [12], and then we describe the experimentally achievable "soft" regime, where although the ground state degeneracy is lifted, the qubit states are exponentially protected against

relaxation and charge-noise-induced dephasing and first order protected against flux noise.

The original 0–π circuit consists of identical pairs of small Josephson junctions, large shunting capacitors, and superinductors, which are all organized in a single closed-loop geometry with four nodes as shown in Fig. 1(a). Accordingly, the circuit has three relevant degrees of freedom and a center-of-mass mode [17], which we refer to as the θ, ϕ, ζ, and Σ modes, respectively. These modes correspond to linear combinations of the phase differences of the superconducting order parameter across various elements in the circuit [Fig. 1(b)]. Among them, the Σ mode is cyclic, and the ζ mode represents a harmonic mode that is decoupled from the other circuit modes in the absence of circuit-element disorder. The remaining θ and ϕ modes, which in the noise-protected regime correspond to delocalized charge and flux modes, respectively, describe the qubit degrees of freedom of the circuit with the following two-mode Hamiltonian:

$$
\begin{aligned}
H_{0-\pi} = {} & 4E_C^\theta (n_\theta - n_g^\theta)^2 + 4E_C^\phi n_\phi^2 \\
& - 2E_J \cos\theta \cos\left(\phi - \frac{\pi \Phi_{\text{ext}}}{\Phi_0}\right) + E_L \phi^2, \quad (1)
\end{aligned}
$$

where $E_C^\theta = e^2/2C_\theta$ ($E_C^\phi = e^2/2C_\phi$) denotes the charging energy corresponding to the θ (ϕ) mode with total capacitance C_θ (C_ϕ), E_J is the Josephson energy, $E_L = \Phi_0^2/4\pi^2 L$ is the inductive energy of the superinductor with inductance L, $\Phi_0 = h/2e$ is the magnetic flux quantum (with electron charge e and Planck's constant h), Φ_{ext} is the external magnetic flux threaded through the loop of the device, n_g^θ is the offset-charge bias due to the electrostatic environment, and n_θ and n_ϕ are the canonical charge operators (in the unit of $2e$) corresponding to the phase operators θ and ϕ, respectively. In quantum electromagnetic circuits [29], the capacitive energies of the device determine the kinetic energies of the modes, while the inductors and Josephson junctions underpin the staggered double-well potential of the qubit, illustrated in Fig. 1(c).

Remarkably, the three bosonic modes of the 0–π circuit correspond to the three fundamental representatives of superconducting qubits: the transmon [26], the fluxonium [30], and the cavity [31]. Indeed, as Fig. 1(b) shows, the θ mode describes the superconducting phase difference across the large shunting capacitors and the Josephson junctions, leading to transmonlike behavior. On the other hand, the ϕ mode corresponds to the phase drop across the Josephson junctions and the superinductors, which features a fluxonium-type response. Finally, the ζ mode arises from the phase difference across the superinductances and the shunting capacitors, resulting in a low-energy harmonic mode.

As the protection of the 0–π qubit emerges from the interplay of its effective double-well potential and the anisotropic kinetic energy of the modes [11,12,17–19],
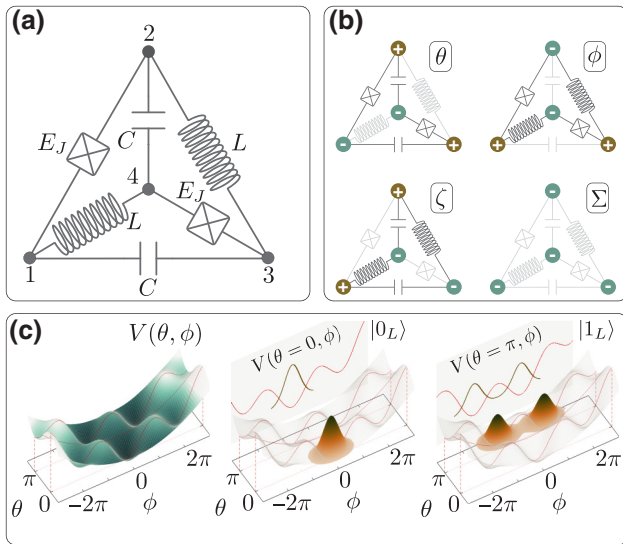
FIG. 1. (a) The circuit diagram of the 0–π qubit [11,12], which is identical to the soft 0–π circuit. The circuit has one closed loop with four nodes connected by a pair of Josephson junctions (E_J), large capacitors (C), and superinductors (L). (b) The four modes of the circuit with colors of the nodes indicating the sign of normal-mode amplitudes. (c) Left panel: the $V(\theta,\phi)$ double-well potential landscape of the soft 0–π circuit in the absence of magnetic fields. Middle and right panels: the wave functions of the logical qubit states are localized along the $\theta = 0, \pi$ valleys. The line cuts along the two valleys in the ϕ direction show that the potential resembles a fluxonium potential.

engineering the proper energy scales in the qubit is crucial. We first consider the case of protection against energy relaxation, which is provided by localizing the qubit wave functions in either the $\theta = 0$ valley or the $\theta = \pi$ valley [see Fig. 1(c)]. The circuit realizes an effective double-well potential with two fluxoniumlike potentials, $V(\phi, \theta = 0, \pi) = \mp 2E_J \cos\phi + E_L\phi^2$, along the 0 and π valleys at $\Phi_{ext} = 0$. The two potentials are displaced with respect to each other such that the $\theta = 0$ valley has a single minimum at $\phi = 0$, whereas the $\theta = \pi$ valley features two minima at $\phi \simeq \pm\pi$. Importantly, the potential energy difference ($E_L\pi^2$) between the minima of the 0 and π valleys corresponds approximately to the transition frequency between the lowest-lying states of the two valleys (i.e., the qubit energy). To ensure that the logical excited state is localized along the θ direction, first, the effective barrier height separating the valleys (approximately $4E_J$) is required to be much larger than the qubit transition energy, which we realize with $E_J/E_L \approx 16$ in the soft 0–π version. Second, we choose $E_J/E_C^\theta \approx 65$, as the tunneling amplitude between the valleys is exponentially reduced with the ratio of barrier height and kinetic energy [26].

Since the qubit couples to the charge and flux degrees of freedom of the environment through the θ charge and ϕ flux modes, respectively, we achieve protection from charge fluctuations and flux fluctuations by combining the

beneficial parameter regimes of the transmon and fluxonium qubits (see Appendix E for detailed discussion). First, to exponentially suppress the charge sensitivity of the qubit, we simply operate the θ mode in the transmon regime. Second, to overcome flux sensitivity, we exploit the avoided crossing of the two lowest-lying levels of the $\theta = \pi$ valley to engineer a first-order-insensitive flux sweet spot [30]. Indeed, the $\phi \to -\phi$ symmetry at $\Phi_{ext} = 0$ accompanied by two local minima in the potential of the π valley [Fig. 1(c), right panel] results in pairs of symmetric and antisymmetric states. Such hybridized states show a hyperbolic dispersion as a function of external flux and a first-order-insensitive sweet spot at zero field. The magnitude of the avoided crossing and consequently the protection against flux noise is proportional to the tunneling rate between the two local minima of the π valley, therefore requiring a sufficiently large E_C^ϕ. Ultimately, the θ mode is heavy due to the small charging energy E_C^θ and the ϕ mode is rendered light owing to the large E_C^ϕ value. Such an anisotropic kinetic energy ratio of $E_C^\phi/E_C^\theta \approx 12$ ensures that the θ mode is delocalized in charge space and the ϕ mode is delocalized in phase space. Because of the limitations of current superconducting-qubit technologies, (i.e., the presence of parasitic capacitances), our parameter regime is relaxed compared with the original 0–π qubit proposal [11,12] as it realizes a smaller degree of delocalization for the ϕ mode; consequently, the exponential protection against flux noise [12] is reduced to first-order protection at a sweet spot in our device.

Figure 2 shows the energy spectrum and wave functions of the soft 0–π circuit in the absence of external magnetic fields. In the $\theta = 0$ valley, the excitations are plasmon-like with wave functions similar to those of an anisotropic, two-dimensional harmonic oscillator. The nodes of the wave functions appear first along the θ direction, as the kinetic energy of the θ mode is much lower than that of the ϕ mode. In the $\theta = \pi$ valley, the eigenstates appear in symmetric-antisymmetric pairs, with nodes again developing first along the θ direction. Inspired by the quantum numbers of natural atoms, we denote low-lying energy levels as $|n_{lm}^j\rangle$, where the first quantum number $n = 0, \pi$ refers to the valley index, $l = s, p, d, f \ldots$ specifies the number of the nodes of the wave function, and $m = \theta, \phi$ determines the orientation of the nodes (if any). Finally, for the states in the π valley, the superscript $j = +, -$ refers to the ϕ parity of the state. In this work, we use the lowest-energy states of the two valleys, $|0_s\rangle$ and $|\pi_s^+\rangle$, as the logical qubit states.

III. EXPERIMENTAL IMPLEMENTATION OF THE PROTECTED CIRCUIT

We fabricate the device using conventional lithographic techniques in a two-dimensional circuit-QED architecture (see Appendix A). The qubit is capacitively coupled
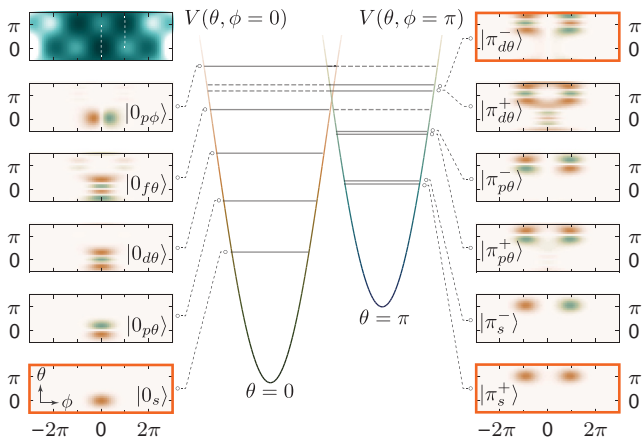
FIG. 2. The two-dimensional wave functions of the eigenstates of the soft 0–π circuit, which are located mostly in the $\theta = 0$ valley (left panel) or the $\theta = \pi$ valley (right panel). Middle panel: line cuts of the potential along $\phi = 0$ and $\phi = \pi$ as indicated with dashed white lines on the image of the potential (top of left panel). Orange boundaries highlight the logical qubit states and the ancillary level. The wave functions and potential correspond to the parameter regime of the fabricated device.

FIG. 3. False-color image of the soft 0–π device with colors referring to the four nodes of the circuit. Enlarged images illustrate the Dolan-type single Josephson junctions (JJs) and part of the Josephson junction arrays used in the device. GND, ground plane of the resonator; V_0, center pin of the resonator.

to a coplanar-waveguide cavity with resonant frequency $\omega_c/2\pi = 7.328$ GHz and photon decay rate $\kappa/2\pi = 1.6$ MHz, which enables us to probe the qubit by dispersive readout [32,33]. As Fig. 3 shows, our primary goal for the circuit layout is to implement the highly anisotropic nature of the kinetic energies of the θ and ϕ modes with two tightly interdigitated niobium capacitors placed at a large distance from each other. Although this design increases the susceptibility of the device to dielectric losses due to the extremely small gap between the capacitor fingers (600 nm), it reduces the cross capacitances contributing to the mass of the light ϕ mode while maintaining a large enough capacitance ($C = 101$ fF) for the heavy θ mode, yielding $E_C^\theta/h = 92$ MHz and $E_C^\phi/h = 1.14$ GHz. The two small Josephson junctions are double-angle-evaporated Al-AlO$_x$-Al Dolan-type junctions with $E_J/h = 6.0$ GHz. Each superinductor is realized by an array of 199 large Josephson junctions, resulting in $E_L/h = 0.38$ GHz. We choose an asymmetric resonator-coupling scheme where all four nodes of the qubit have considerable coupling capacitance to both the center pin of the resonator and the ground plane, which allows us to address both the ϕ mode and the θ mode in our measurements (see Appendix B). The values of these coupling capacitances are carefully chosen to realize sufficiently large coupling rates for qubit operation without our significantly increasing the capacitances associated with the ϕ mode. Additionally, dc voltage biasing of the center pin of the resonator allows us to tune the offset charges on the islands of the device.

To map out the energy spectrum, we perform standard two-tone spectroscopy as a function of external magnetic
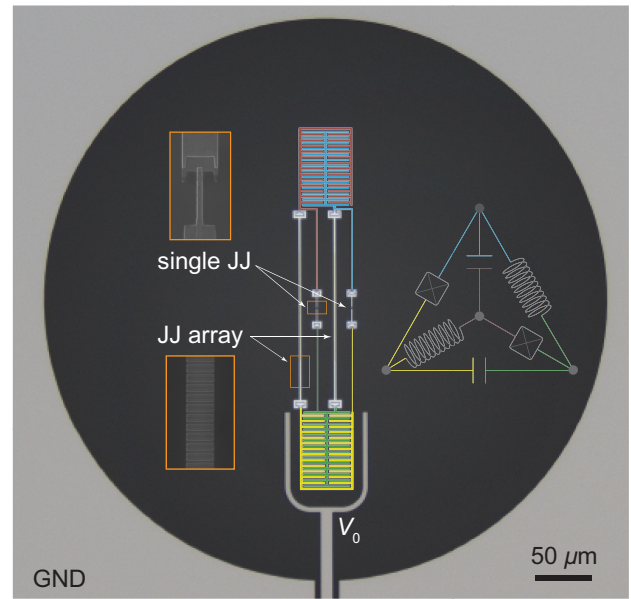
flux and offset-charge bias. In the dispersive limit of circuit QED [32,33], we can probe the excitation of various transitions by monitoring the transmission at the cavity frequency while sweeping the frequency of a second spectroscopic tone (Fig. 4). As expected, the spectroscopic data obtained as a function of flux reveal two types of transitions: intravalley plasmon transitions in the 0 valley, which are characterized by flat, almost flux-independent dispersion [white arrows in Figs. 4(a) and 4(b)], and intervalley fluxon excitations between the 0 and π wells, which have strong flux dependence [black arrows in Figs. 4(a) and 4(b)]. The offset-charge biases $n_g^\theta = 0$ and $n_g^\theta = 0.5$ are superimposed in the spectroscopy measurement [Fig. 4(a)], as at these bias values we simultaneously observe the two sets of transitions due to the intermittent tunneling of unpaired quasiparticles across the junctions [34–38]. By contrast, at $n_g^\theta = 0.25$ [Fig. 4(b)], we observe only one set of transitions, which indicates the insensitivity of the qubit to individual quasiparticle tunneling events. This behavior is more apparent when we measure the qubit spectrum as a function of n_g^θ [Fig. 4(c)]. At low energies, the transmonlike excitations have exponentially suppressed charge dispersion [26,35], and we are unable to resolve the different states corresponding to an even or odd number of quasiparticles. At higher frequencies, however, eyelike patterns appear with dispersions up to approximately 1 GHz due to the strong charge sensitivity of the higher-lying levels.
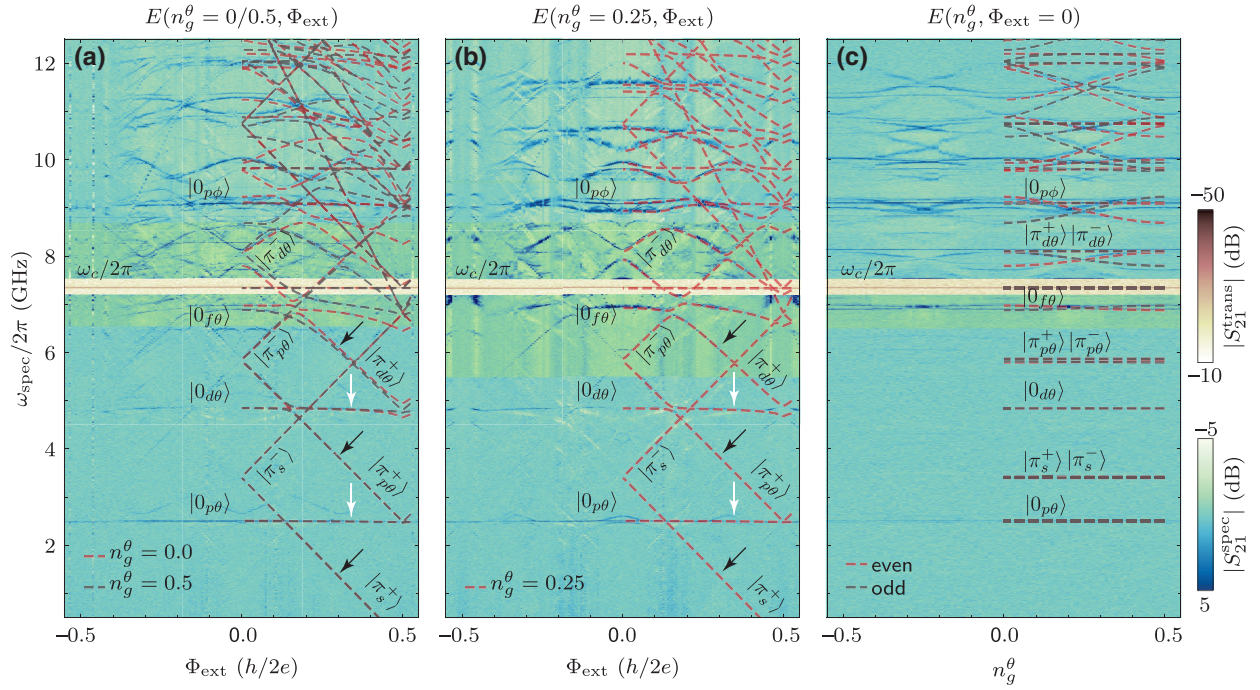
FIG. 4. Transmission and spectroscopy measurements (background subtracted) of the soft 0–π qubit (a) at $n_g^\theta = 0.0/0.5$ and (b) at $n_g^\theta = 0.25$ as a function of external magnetic field and (c) at $\Phi_{\text{ext}} = 0$ as a function of offset-charge bias. The transmission measurements around 7.3 GHz (yellow-brown) and the spectroscopic data (green-blue) demonstrate excellent agreement with a coupled resonator-qubit theoretical fit (dashed lines). The result of the fit is plotted over only the positive side of the data for clarity. The low-energy fluxon transitions are not visible in the spectroscopy data due to the small dipole elements. Black and white arrows indicate the fluxon and plasmon transitions, respectively. The additional features can be explained by sideband transitions or excitations of higher-lying states (see Appendix C for details).

It is worth emphasizing that we find remarkable agreement between the simple two-mode Hamiltonian in Eq. (1) of the qubit and the experimental data over the entire range of both offset charge and external flux. This relatively simple theoretical model not only captures accurately the energy-level structure with at least 17 transitions over a 12-GHz frequency range but also predicts the cavity-assisted sideband transitions and qubit transitions due to thermal occupation of low-lying levels (see Appendix C). This excellent agreement highlights that although the soft 0–π artificial atom is constructed from the combination of 400 Josephson junctions and large capacitors, its effective dynamics are fairly simple, which is highly favorable for a qubit to be implemented in a large-scale quantum processor.

IV. MAPPING THE LOGICAL STATES

Owing to the exponentially small dipole matrix element between the logical qubit states, direct transitions between these states with disjoint support are strongly suppressed. To control the qubit, we therefore take advantage of higher-energy states that have support in both valleys. In

particular, we choose the $|\pi_{d\theta}^-\rangle$ state as the ancillary level (Fig. 2), which has reduced charge sensitivity and finite coupling to both logical qubit states.

First, to unambiguously demonstrate the existence of the logical states, we perform multitone spectroscopy between the lowest-lying states of the valleys ($|0_s\rangle$, $|\pi_s^+\rangle$, $|\pi_s^-\rangle$) and the ancillary level $|\pi_{d\theta}^-\rangle$, which form a double-Λ configuration [Fig. 5(a), inset]. By irradiating the qubit with a strong coupler drive near the $|\pi_{d\theta}^-\rangle \leftrightarrow |\pi_s^\pm\rangle$ transitions and weakly probing the $|0_s\rangle \leftrightarrow |\pi_{d\theta}^-\rangle$ transition, we resolve two avoided crossings [Fig. 5(a)], each of which is also referred to as an Autler-Townes doublet [39–41]. These correspond to the dressed states associated with the fluxon transitions of the lowest-lying symmetric $|\pi_s^+\rangle$ and anti-symmetric $|\pi_s^-\rangle$ states. At finite detunings from the ancillary level, we observe the signature of stimulated Raman transitions as a pair of lines with a slope of +1 when the frequency difference of the probe and coupler tones is on resonance with the transition $|0_s\rangle \leftrightarrow |\pi_s^-\rangle$ or $|0_s\rangle \leftrightarrow |\pi_s^+\rangle$. In the vicinity of $\Phi_{\text{ext}} = 0$ [Fig. 5(b)], the Raman transitions allow us to map out the hybridization gap formed between the lowest-lying states $|\pi_s^\pm\rangle$ of the $\theta = \pi$ valley. The spectroscopy data showcase a magnetic flux sweet spot and a hybridization gap of $\Delta_H/2\pi \approx 20$ MHz. These
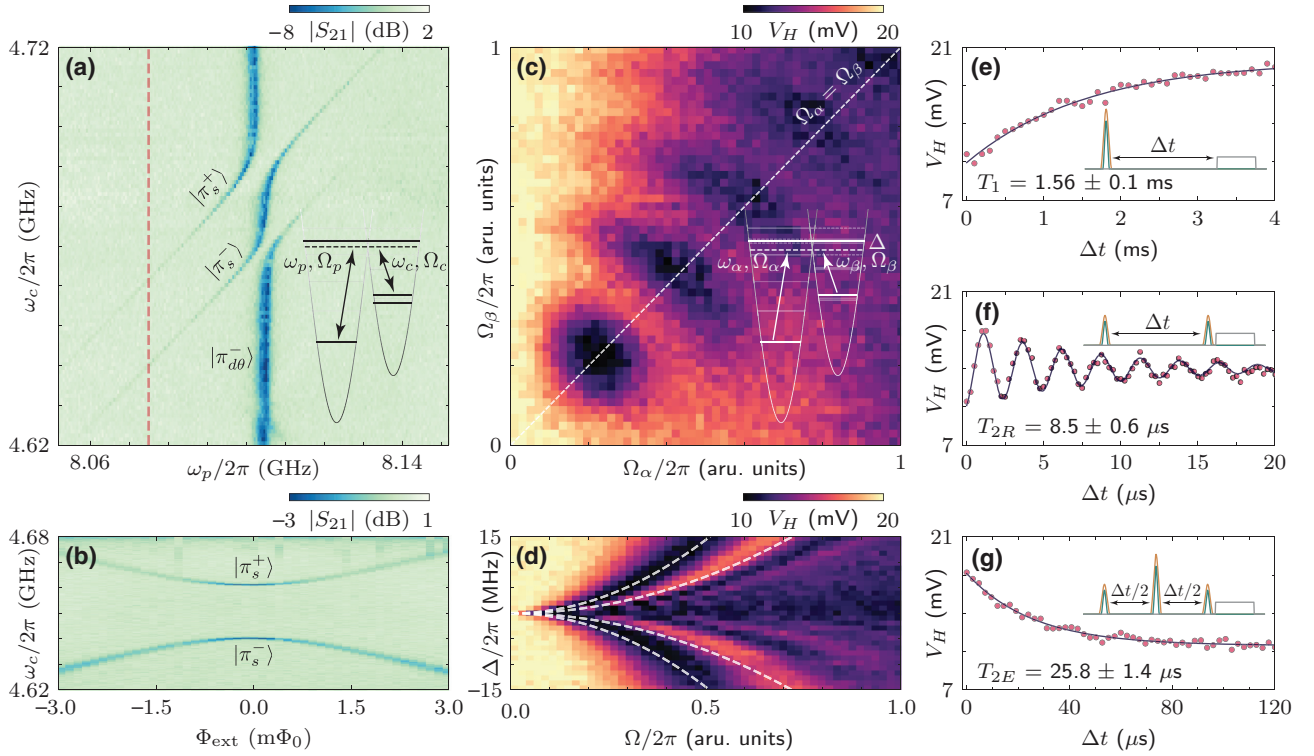
FIG. 5. (a) Autler-Townes spectroscopy (background subtracted) between the ground states of the qubit using the ancillary $|\pi^-_{d\theta}\rangle$ level. The inset shows the continuous drive scheme. (b) Raman spectroscopy at detuning $\Delta/2\pi = -30$ MHz from the ancillary level [dashed red line in (a)] as a function of external magnetic field, which demonstrates a magnetic sweet spot for the disjoint ground states. (c),(d) Coherent Rabi oscillations between the logical states $|0_s\rangle$ and $|\pi^+_s\rangle$ obtained by use of two overlapping Gaussian pulses with width of 4σ. (c) The measured homodyne voltage V_H as a function of drive amplitudes at a fixed detuning ($\Delta/2\pi = -3$ MHz, $\sigma = 1$ μs), and (d) V_H as a function of detuning at equal drive amplitudes ($\Omega_1 = \Omega_2$, $\sigma = 0.8$ μs). The maximum population transfer occurs when the two drive amplitudes are equal. The dashed lines in (d) show a fit according to the effective Rabi rate of the Raman pulses. (e)–(g) Relaxation, Ramsey, and spin-echo measurements of the logical states, with insets showing the pulse scheme ($\Delta/2\pi = -4$ MHz and $\sigma = 200$ ns). All data are taken at the $n^\theta_g = 0.25$ charge-bias point.

V. COHERENT CONTROL OF THE LOGICAL STATES

We achieve coherent control of the qubit states using Raman gates again via $|\pi^-_{d\theta}\rangle$. To coherently transfer the population between the $|0_s\rangle$ and $|\pi^+_s\rangle$ logical ground states, we use two simultaneous Gaussian-shaped pulses with amplitudes Ω_α and Ω_β (see Appendix G for details). The frequencies of the pulses link the two logical states via the ancillary level, and have a detuning of $\Delta/2\pi$ from $|\pi^-_{d\theta}\rangle$ [Fig. 5(c), inset]. In this Raman scheme, the two pulses and the truncated three-level system exhibit an effective two-level dynamics, where during the pulse only a very small fraction of the population occupies the unprotected intermediate state. In this way, we demonstrate Rabi oscillations between the logical states by first fixing the detuning of the pulses and independently varying the amplitudes of the two drives [Fig. 5(c)]. In this protocol [42], complete population transfer can be realized when the two amplitudes are equal ($\Omega_\alpha = \Omega_\beta$). In Fig. 5(d), we show coherent manipulation by keeping equal drive amplitudes ($\Omega_\alpha = \Omega_\beta = \Omega$) and varying the detuning Δ from the intermediate level, which results in oscillations in good agreement with an effective Rabi amplitude $\Omega_R \propto \Omega^2/\Delta$ [43].

These time-domain measurements allow us to find the amplitudes of the Gaussian pulses with $\sigma = 200$ ns (and total duration of $4\sigma = 800$ ns) for the π and $\pi/2$ pulses between the logical qubit states to characterize their lifetime and coherence [Figs. 5(e)–5(g)]. The slow gates in the current device are the consequence of the strong filtering of the readout cavity, which reduces the power transmitted to the qubit and prohibits us from realizing shorter pulses with higher amplitude. The gate operation time can be reduced significantly by use of separate gate lines or fast-flux lines. Energy relaxation measurements reveal $T_1 = 1.56 \pm 0.1$ ms (see Appendix D), while
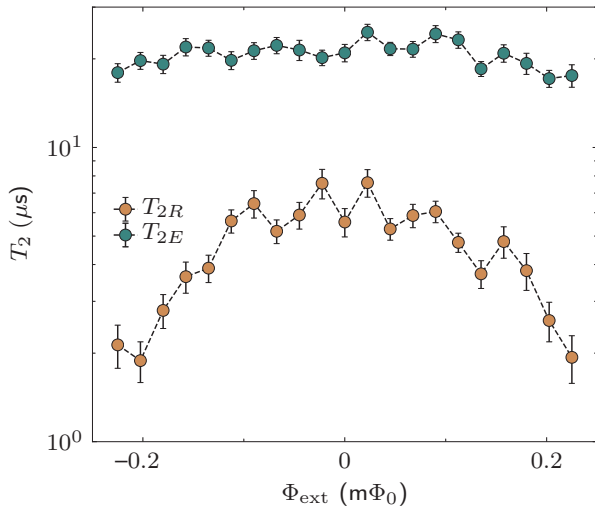
measurements demonstrate that the qubit states are first order protected against flux noise.

FIG. 6. Measured T_{2R} and T_{2E} values around the magnetic sweet spot $\Phi_{\text{ext}} = 0$. Dashed lines are a guide for the eye. The data show that the Ramsey coherence times have strong dependence on Φ_{ext}, with a significant enhancement around the sweet spot, demonstrating first-order insensitivity of the coherence time to fluctuations of the external magnetic flux.

Ramsey interferometry and Hahn echo experiments yield $T_{2R} = 8.5 \pm 0.6$ μs and $T_{2E} = 25.8 \pm 1.4$ μs, respectively (at $\Phi_{\text{ext}} = 0$). By performing T_{2R} and T_{2E} measurements in the vicinity of the qubit's operating point, we also demonstrate first-order protection against flux-noise dephasing (see Fig. 6).

VI. DISCUSSION AND OUTLOOK

The 0–π circuit has a unique position among superconducting qubits as it promises simultaneous protection against energy relaxation and pure dephasing, a feature that none of the previously developed superconducting devices have. The "mainstream" superconducting qubits are robust with regard to either longitudinal noise (in the case of the transmon [44] and the fluxonium [45]) or transverse noise (in the case of the "heavy" fluxonium capacitively shunted away from the half-flux quantum [23,24]). To achieve superior coherence times, however, a qubit must be protected against both noise channels. Since the logical qubit states of the circuit have wave functions with disjoint support and energy levels that are insensitive to flux and offset charge, this qubit offers a hardware-efficient platform to realize an intrinsically protected superconducting qubit.

Importantly, the experimental realization of such a multinode device has limitations that hinder the full potential of the theoretically proposed 0–π qubit. Here we discuss the three main challenges that must be overcome to consider the soft 0–π qubit as a prime candidate for a quantum processor. These limitations arise mostly from the constraints in current fabrication procedures and the available material platforms for superconductor-based electronics.

First, we recall that the energy scales of our qubit are relaxed compared with the original proposal due to the unavoidable stray capacitances across various parts of the circuit. These unwanted capacitances undermine the realization of an ultralight flux mode in the circuit. A layered three-dimensional capacitor structure and high-kinetic-inductance materials with high plasma frequency could help to mitigate this problem. The advantage of the three-dimensional, overlap capacitor pack is its small footprint, which reduces the capacitance between a node that is part of the given capacitor and a node that is not included in it. This requires the development of low-dielectric-loss materials as part of the capacitor or vacuum-gapped capacitors [46], which also provides motivation for the use of *in situ*–fabricated two-dimensional superconductor-based structures. Our device realizes the heavy charge mode, but the "lightness" of the flux mode falls short of the original proposal, resulting in exponential protection against charge noise but only first-order protection against flux noise. In this parameter regime, the coupling between the $\theta = 0$ and $\theta = \pi$ valleys is stronger and finding the correct values of circuit components is more critical: choosing a parameter set that provides a high degree of protection against charge noise exposes the device to flux noise and vice versa. We provide a detailed analysis in Appendix E of how we find the balance between relaxation, charge, and flux sensitivity.

The second important aspect to consider is the presence of disorder in the circuit elements due to imperfect fabrication of aluminum oxide–based Josephson junctions. When the pairs of superconducting elements are not identical in the 0–π qubit, the charge and flux modes dispersively couple to the low-energy harmonic ζ mode. In our device, the frequency of the ζ mode is around 753 MHz, which can be detected in a spectroscopic measurement [Fig. 7(a)]. Because of the thermal occupation of this mode, photon shot noise can limit the performance of the qubit [28]. However, quantifying the impact of photon-number fluctuations in the thermal occupation of the low-energy ζ mode on the pure-dephasing time is challenging because it requires a precise estimation of the dispersive shift of the logical qubit transition due to spurious coupling to the ζ mode. Indeed, relying on a purely theoretical analysis (see Appendix F for details), we estimate that this dispersive shift is on the order of 1–10 kHz, and thus is difficult to resolve experimentally. Nevertheless, in Fig. 7(b) we provide a theoretical estimate for the pure dephasing times of the qubit due to the photon-shot-noise dephasing at different degrees of disorder values as a function of the temperature of the ζ mode. For this reason, further experimental work will focus on characterizing the coupling to the ζ mode in order to accurately quantify its effect on
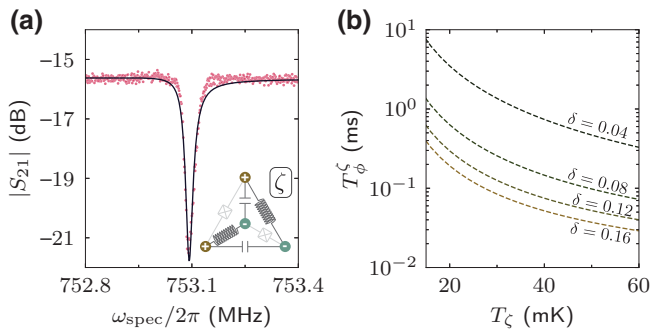
FIG. 7. (a) The spectroscopic response of the harmonic ζ mode. The solid line shows the fit [47] with quality factors $Q_{\text{ext}}^{\zeta} = 41\,600$ and $Q_{\text{int}}^{\zeta} = 42\,500$. (b) Theoretical estimate of the pure dephasing rate due to thermal photon shot noise as a function of disorder $\delta = \delta A/A$ of Josephson junction areas A and the temperature of the ζ mode T_ζ. The disorder of the inductors realized by N Josephson junctions is assumed to follow $\delta E_L/E_L = \delta/\sqrt{N}$.

qubit coherence and explore the viability of cooling this mode [19].

Finally, we point out that further increase of the speed of gate operation is highly important for our circuit. Currently, the limitation arises from the small coupling rates between the states, from the small hybridization gap (20 MHz) between the first two states in the π valley (Fig. 2), and because the drive tones are sent through the readout cavity. The speed of the gate can be increased, for example, by carefully changing the parameters of the device such that the dipole coupling and the hybridization gap between the levels are increased (see Appendix E for a detailed discussion). This ultimately requires us to find the optimal parameter values depending on the noise amplitudes. Additionally, implementing gates that are on-resonant with the ancillary level [48] and parametric gates with additional gate or fast-flux lines [49] and taking advantage of optimal control techniques [50] will lead to significant improvements in future demonstrations.

Our work demonstrates the first experimental realization of a superconducting qubit, which is exponentially protected against energy relaxation and charge noise, and first order protected against flux noise, opening new avenues for robust encoding of quantum information in artificial atoms. This is reflected by the measured relaxation time, which is a half an order of magnitude increase over that of current state-of-the-art transmons [44] and comparable to the results reported for highly-flux-sensitive capacitively shunted "heavy" fluxonium qubits with metastable states [23,24]. Moreover, the measured coherence times represents about an order of magnitude increase with respect to the values reported for qubits with disjoint support [23,24]. The critical component of the realized qubit is the presence of a higher-lying, charge-insensitive ancillary state that is not only beneficial for Raman-type single-qubit gates

but also opens up the possibility to use noncomputational states as the basis for two-qubit gates between protected qubits [51,52]. Although further efforts are required to improve the gate performance and the decoupling of the device from photon shot noise, at the current level, such a "biased" qubit with a long relaxation time and average coherence time can be considered as a candidate for memory units in a quantum processor. Additionally, it has the potential to improve the performance of bosonic codes [53,54], given the large dispersive shifts between the logical states, and the realized device provides a platform for simulation of solid-state systems and the exploration of fundamental physical phenomena [55,56].

APPENDIX A: SAMPLE FABRICATION AND MEASUREMENT SETUP

The device is fabricated on a 530-μm-thick, polished *c*-plane sapphire substrate, on which 200 nm of niobium is sputtered. We use optical lithography to define the resonators and shunting capacitances and dry etching using a mixture of CHF$_3$, O$_2$, SF$_6$, and Ar gases (with 40:1:15:10 ratio). We expose the Josephson junctions in a 125-keV Elionix electron-beam system (at a beam current of 1 nA and 60-μm aperture). The Josephson junctions are double angle evaporated in a Plassys electron-beam-evaporator system with base pressure less than 10^{-7} mbar. Before the evaporation, an *in situ* argon ion beam etch is used to clean the surface of the sample. We evaporate 20-nm-thick Al (first layer) plus 50-nm-thick Al (second layer) at 0.4 nm/s and oxidize the first layer for 10 min at 200 mbar in a 15% oxygen-in-argon environment to realize the tunnel junction.

The device is mounted on a copper printed circuit board and wire-bonded (Fig. 8). An off-chip copper coil is attached to the printed circuit board. The sample holder has an aluminum shield (covered with Eccosorb CR-124 and
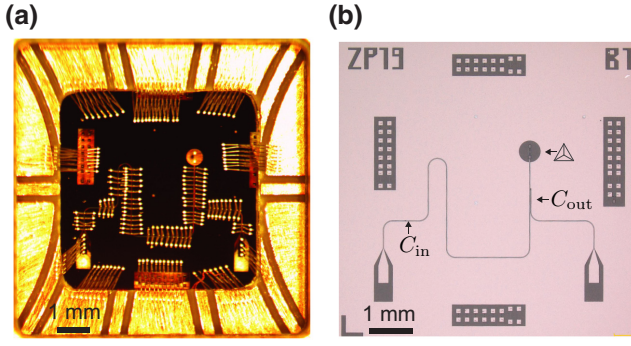
FIG. 8. (a) Optical image of a wire-bonded device mounted into the sample holder. (b) Image of the 7×7 mm^2 chip showing the resonator with its coupling capacitors and the qubit.

wrapped with thin Mylar layers) and an outer mu-metal shield. The sample holder is attached to the mixing chamber plate of a dilution refrigerator with a base temperature of 10 mK (Fig. 9).

APPENDIX B: FINITE-ELEMENT SIMULATION

As mentioned in the main text, realizing the proper capacitance values in the soft 0–π circuit is a key requirement to achieve the parameter regime for noise protection. The large shunting capacitance in the circuit is denoted by C, while the cross capacitance between the nodes enclosing the superinductances (Josephson junctions) is C_L^x (C_J^x). In our design, all four nodes are coupled to both the center pin (C_r^i) and the ground plane (C_0^i) of the resonator (Fig. 10). We use ANSYS MAXWELL electromagnetic field simulation software to determine the capacitance values in the circuit, which are summarized in Table I. These parameters (with the assumptions of dielectric constant $\epsilon_r = 10.7$ for sapphire, $C_J = 2$ fF, and $E_L = 0.38$ GHz) result in energy scales of $E_C^\theta/h = 88$ MHz, $E_C^\phi/h = 1.02$ GHz, and $\omega_\zeta/2\pi = 742$ MHz, which are in excellent agreement with our experimental findings.

APPENDIX C: SPECTRUM FIT

Here we describe the multivariate fit to the experimental data based on a detailed theoretical model for the 0–π device. We consider the circuit scheme in Fig. 10, where we have introduced additional gate (C_r^i) and ground (C_0^i) capacitances for nodes $i \in [1, 4]$. In the flux node basis $\{\Phi_i\}$, the circuit Lagrangian takes the form

TABLE I. Finite-element simulation of the device capacitances. All values are given in femtofarads.

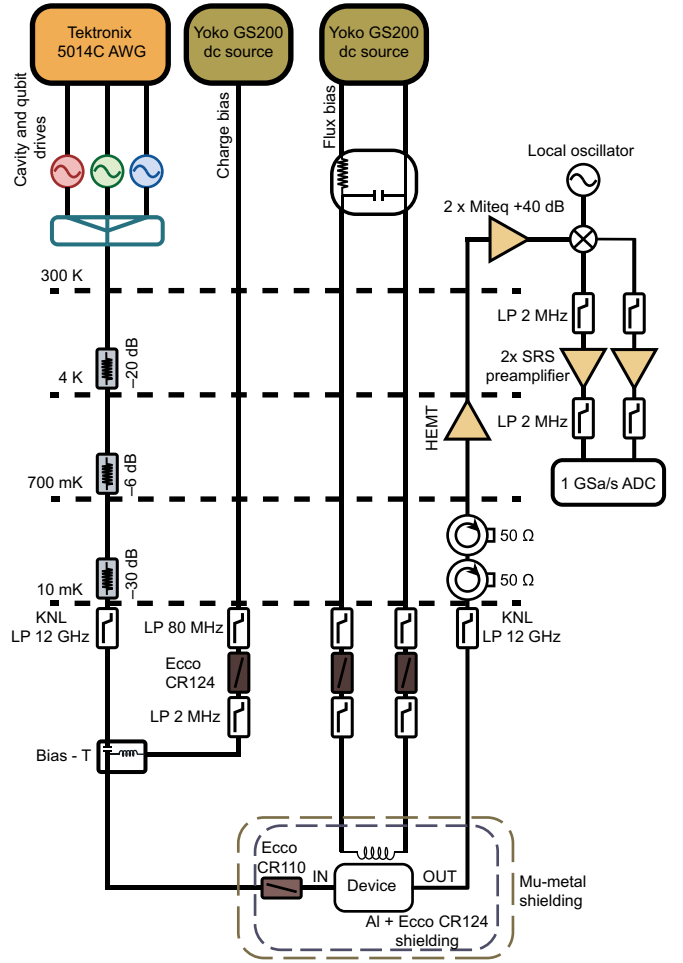| C	C_L^x	C_J^x	C_r^1	C_r^2	C_r^3	C_r^4	C_0^1	C_0^2	C_0^3	C_0^4
100.5	0.7	1.0	9.1	0.3	3.8	0.3	8.2	7.9	6.2	11.6

FIG. 9. Wiring diagram of the cryogenic- and room-temperature measurement setup. ADC, analog-to-digital converter; AWG, arbitrary waveform generator.

$$\mathcal{L}_\Phi = \dot{\Phi}^T \cdot \frac{\mathbf{C}_\Phi}{2} \cdot \dot{\Phi} - \dot{\Phi}^T \cdot \mathbf{C}_r \cdot \mathbf{V}_\Phi - U(\Phi, \Phi_{\text{ext}}), \quad \text{(C1)}$$

where $\Phi = (\Phi_1, \ldots, \Phi_4)^T$, $\mathbf{C}_\Phi$ is the capacitance matrix of the circuit (including gate and ground capacitances), $\mathbf{V}_\Phi = V_r(1, 1, 1, 1)^T$ is a voltage-drive vector defined in terms of the resonator voltage, V_r, $\mathbf{C}_r = \text{diag}(C_r^1, \ldots, C_r^4)$ is the gate capacitance matrix, and $U(\Phi, \Phi_{\text{ext}})$ is the potential energy corresponding to the Josephson junctions and inductances of the circuit. More precisely, the capacitance matrix of the circuit is given by

$$\mathbf{C}_\Phi = \begin{pmatrix} C_1 & -C_J & -C & 0 \\ -C_J & C_2 & 0 & -C \\ -C & 0 & C_3 & -C_J \\ 0 & -C & -C_J & C_4 \end{pmatrix}, \quad \text{(C2)}$$

where $C_i = C_J + C + C_r^i + C_0^i$ for $i \in [1, 4]$. We now move to the 0–π mode basis defined by $\Theta = (\phi, \theta, \zeta, \Sigma)^T$,
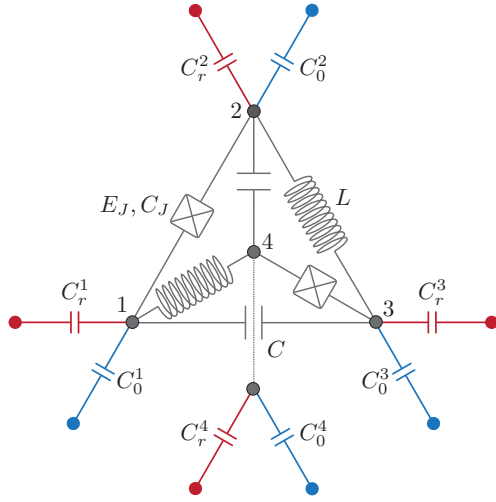
FIG. 10. Full capacitance network of the device. Red and blue indicate coupling to the center pin and ground plane, respectively, of the resonator.

by defining $\Theta = \mathbf{R} \cdot \Phi$, where

$$\mathbf{R} = \frac{1}{2} \begin{pmatrix} -1 & 1 & -1 & 1 \\ -1 & 1 & 1 & -1 \\ 1 & 1 & -1 & -1 \\ 1 & 1 & 1 & 1 \end{pmatrix}. \quad (C3)$$

Under such a transformation, Eq. (C1) becomes

$$\mathcal{L}_\Theta = \dot{\Theta}^T \cdot \frac{\mathbf{C}_\Theta}{2} \cdot \dot{\Theta} - \dot{\Theta}^T \cdot \tilde{\mathbf{C}}_r \cdot \mathbf{V}_\Theta - U(\Theta, \Phi_{\text{ext}}), \quad (C4)$$

where $\mathbf{C}_\Theta = (\mathbf{R}^{-1})^T \cdot \mathbf{C}_\Phi \cdot \mathbf{R}^{-1}$ and $\tilde{\mathbf{C}}_r = (\mathbf{R}^{-1})^T \cdot \mathbf{C}_r \cdot \mathbf{R}^{-1}$ are the transformed capacitance matrices, and $\mathbf{V}_\Theta = \mathbf{R} \cdot \mathbf{V}_\Phi$ is the voltage-drive vector expressed in the 0–π mode basis. By performing a Legendre transformation, we arrive at the circuit Hamiltonian

$$H = (\mathbf{q}_\Theta + \tilde{\mathbf{C}}_r \cdot \mathbf{V}_\Theta)^T \cdot \frac{\mathbf{C}_\Theta^{-1}}{2} \cdot (\mathbf{q}_\Theta + \tilde{\mathbf{C}}_r \cdot \mathbf{V}_\Theta)$$
$$+ U(\Theta, \Phi_{\text{ext}}), \quad (C5)$$

where $\mathbf{q}_\Theta = \partial\mathcal{L}_\Theta/\partial\dot{\Theta}$ is the conjugate charge vector operator. Equation (C5) can be split as

$$H = H_{0-\pi} + H_{\text{drive}}, \quad (C6)$$

where

$$H_{0-\pi} = \mathbf{q}_\Theta^T \cdot \frac{\mathbf{C}_\Theta^{-1}}{2} \cdot \mathbf{q}_\Theta + U(\Theta, \Phi_{\text{ext}}) \quad (C7)$$
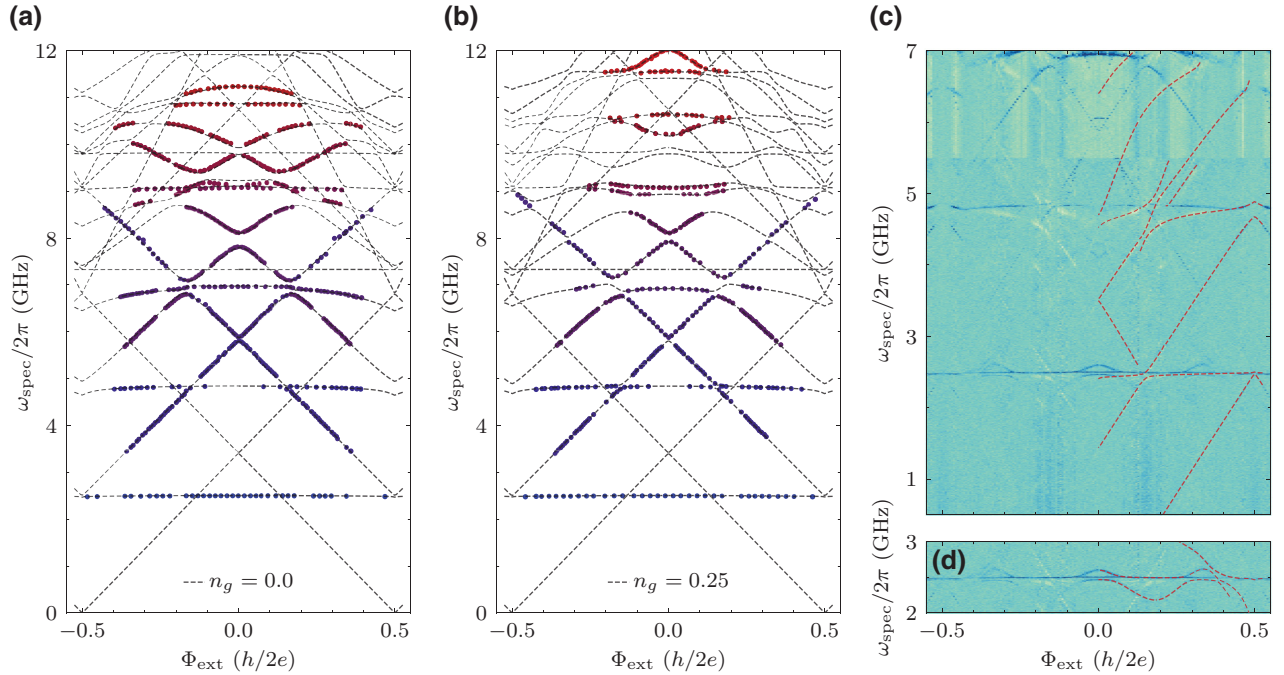

FIG. 11. Spectrum fit of the soft 0–π device at (a) $n_g = 0$ and (b) $n_g = 0.25$. The experimental data used for the fit are displayed by colored circles, while the theortical results are given by the dashed black lines. Some of the qubit transitions are invisible in the experiment due to exponentially small matrix elements or vanishing dispersive shifts. The transition around 7.35 GHz corresponds to the readout resonator. (c) Overlay of the transitions predicted by our model on the experimental data by our assuming thermal population of the lowest two levels in the π valley, which explains the origin of the "bright" transitions in the spectrum ($n_g = 0.25$). (d) A set of cavity-assited red sideband transtions [57] that are also captured by the theoretical model ($n_g = 0.25$). The sideband transitions (dashed lines) are obtained by subtraction of the resonator frequency from the theoretically obtained qubit transition energies.

is the undriven 0–π qubit Hamiltonian and

$$H_{\text{drive}} = \mathbf{q}_\Theta^T \cdot (\mathbf{C}_\Theta^{-1} \cdot \tilde{\mathbf{C}}_r) \cdot \mathbf{V}_\Theta \tag{C8}$$

is a drive term.

While Eq. (C6) takes into account all circuit details, the spectrum fit that is presented in the main text aims to provide the simplest possible accurate description of the device Hamiltonian. Thus, to simplify our treatment, we implement a few approximations. In particular, we omit any coupling to the ζ and Σ modes, ignoring a potential capacitive interaction between these and the qubit modes and reducing the qubit Hamiltonian to

$$H_{0\text{-}\pi} \simeq 4E_C^\phi n_\phi^2 + 4E_C^\theta (n_\theta - n_g)^2 + \hbar g_{\phi\theta} n_\phi n_\theta + U(\Theta, \Phi_{\text{ext}}), \tag{C9}$$

where $E_C^\phi = e^2/2C_\phi$ and $E_C^\theta = e^2/2C_\theta$ are the charging energies of the ϕ and θ modes and $\hbar g_{\phi\theta}$ is the strength of a capacitive interaction between these modes due to the asymmetry of the circuit capacitance matrix. Accordingly, we also approximate Eq. (C8) by

$$H_{\text{drive}} \simeq (\beta_\phi n_\phi + \beta_\theta n_\theta) \times 2eV_r, \tag{C10}$$

where β_ϕ and β_θ are capacitive coupling ratios for the ϕ and θ modes. We moreover set $g_{\phi\theta} \to 0$ in Eq. (C10), eliminating one fit parameter. We observe, however, that deviations from $g_{\phi\theta} = 0$ within bounds given by finite-element estimations of the coupling capacitance do not significantly modify the quality of the fit.

For the multivariate fit, we treat all energy and coupling variables as fit parameters, including E_{C_ϕ}, E_{C_θ}, β_ϕ, β_θ, and those in the potential energy

$$U(\Theta, \Phi_{\text{ext}}) = -2E_J \cos\theta \cos(\phi - \pi\Phi_{\text{ext}}/\Phi_0) + E_L \phi^2$$
$$+ E_J dE_J \sin\theta \sin(\phi - \pi\Phi_{\text{ext}}/\Phi_0), \tag{C11}$$

defined in terms of the junction energy E_J, the superinductance energy E_L, and the relative junction-energy asymmetry dE_J. The fit also incorporates the resonator mode with nominal impedance $Z_r = 50\Omega$ and frequency $f_r \simeq 7.35$ GHz, for which the voltage operator reads

$$V_r = V_{\text{rms}}(a + a^\dagger), \tag{C12}$$

where $V_{\text{rms}} = \sqrt{2hf_r^2 Z_r}$ for a $\lambda/2$ resonator, and a and $a^\dagger$ are the respective harmonic oscillator ladder operators. We diagonalize the Hamiltonian in the charge and phase basis for the θ and ϕ modes, respectively [17]. The fit takes into account two sets of data corresponding to a sweep of the magnetic flux for the offset charges $n_g = 0.0$ and $n_g = 0.25$. A single error metric measures the distance between the result of the exact diagonalization of the qubit-resonator Hamiltonian and the data sets. The result of the

TABLE II. Result of the multivariate fit to the experimental data. All energy parameter values are given in gigahertz.

E_C^ϕ/h	E_C^θ/h	E_J/h	E_L/h	dE_J	β_ϕ	β_θ
1.142	0.092	6.013	0.377	0.1	0.27	6.6×10^{-3}

fit is shown in Figs. 11(a) and 11(b) (in addition to Fig. 2) and the fit parameters are provided in Table II. The values are in excellent agreement with those expected from a finite-element simulation of the device.

We find excellent agreement between the theoretical model and the experimental data, for both $n_g = 0$ and $n_g = 0.25$. As Fig. 2 shows, the parameter values obtained also describe the transitions at $n_g = 0.5$, and generally, the complete offset-charge dependence of the energy levels. Figure 11(c) also shows that additional features in the spectroscopy data can be explained by transitions between thermally occupied fluxon states to higher levels. Furthermore, the theoretical model captures accurately not only the qubit transitions but also the cavity-assisted sideband transitions. Since the latter transitions were not originally taken into account for the fit, this fact provides further confirmation of the validity of the theoretical model.

APPENDIX D: TIME EVOLUTION OF THE RELAXATION TIME

In addition to isolated measurements reported in the main text, we also continuously monitor the relaxation time over a timescale of 1 day (Fig. 12). The results show oscillation and drifts in the relaxation times similar to the behavior observed in other superconducting qubits.

APPENDIX E: THE CHOICE OF PARAMETERS FOR THE DEVICE

We now give our motivation for the particular choice of the energy scales of the soft 0–π qubit. Importantly, we restrict our analysis to a parameter regime that is achievable with current state-of-the-art lithography techniques
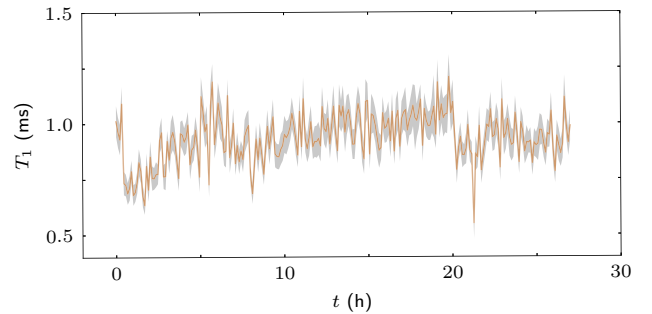

FIG. 12. Measured T_1 values as a function of time. The gray background indicates the error bar of each measurement.

and conventional aluminum oxide–based Josephson junctions. Additionally, we focus on the performance of the qubit at zero external flux.

Our goal is to simultaneously optimize the qubit sensitivity against external charge and flux fluctuations while minimizing dephasing due to shot noise from the ζ mode. Suppressing the effects of these different dephasing mechanisms in experimentally achievable regimes leads to compromises; for example, choosing a parameter set that provides a high degree of protection against charge noise exposes the device to flux noise and vice versa. This is discussed in more detail below.

As a first step, we identify three quantities that determine the susceptibility of the device to various noise sources:

(a) The hybridization gap Δ_H between the lowest-lying symmetric and antisymmetric states of the π valley [see Fig. 13(a)]. We recall that the symmetric state is considered as the logical $|1_L\rangle$ state of our qubit. Thus, Δ_H determines the flux sensitivity of the qubit transition to second order in the amplitude of flux fluctuations at the flux sweet spot. Moreover, a large gap is beneficial for achieving faster gates and avoiding leakage. We therefore aim to maximize Δ_H.

(b) The amplitude t_{01} of the charge dispersion of the qubit transition energy, which indicates the degree of charge sensitivity of the device [Fig. 13(b)] and must be minimized.

(c) The frequency of the harmonic ζ mode $\omega_\zeta/2\pi$, which determines the photon-shot-noise dephasing rate of the qubit. In the soft parameter regime considered in this work, the higher the frequency of the ζ mode, the less sensitive the device is to photon shot noise.

We begin our discussion focusing on the sensitivity of the device to charge noise and flux noise. The susceptibilities of the 0–π qubit to these two dephasing mechanisms have similar origins: the tunneling amplitude between potential minima along the different directions in phase space. First, concentrating on the charge dispersion, we note that localization along the θ direction supports charge-insensitive energy levels similarly to the case of the transmon. This can be understood within a tight-binding picture where the charge dispersion is directly proportional to the tunneling amplitude of localized wave functions between adjacent potential wells [26]. Similarly, delocalization along the ϕ direction increases the size of the hybridization gap, leading to enhanced flux-noise insensitivity. At zero magnetic field, the presence of two minima in the π valley and the $\phi \rightarrow -\phi$ symmetry lead to a pair of symmetric and antisymmetric states. The energy gap between these states is proportional to the tunneling

amplitude along the ϕ direction. As a conclusion, we find that larger tunneling amplitude is mostly favorable along the ϕ direction (the tunneling amplitude increases the hybridization gap Δ_H), whereas it is disadvantageous along the θ direction (the tunneling amplitude increases the charge dispersion t_{01}).

To connect the support in phase space of the qubit states to the parameter scale of the physical device, we recall that quantum tunneling is generally determined by the ratio of the kinetic energy of the state and the effective height of the potential barrier. For example, in the transmon, the tunneling probability of low-lying states follows an approximately $e^{-\alpha\sqrt{E_J/E_C}}$ asymptotic behavior ($\alpha \sim 1$), indicating that increasing the E_J/E_C ratio localizes the qubit states [26]. While obtaining an analytical formula for the two-dimensional case of the qubit is challenging, we can numerically solve the Hamiltonian at different parameter values, leveraging the intuition from the one-dimensional case. Figures 13(c) and 13(d) show, respectively, the hybridization gap and the amplitude of the charge dispersion as a function of kinetic energies E_C^ϕ and E_C^θ. As expected, increasing the kinetic energy increases the tunneling amplitude in both the θ direction and the ϕ direction, leading to a larger hybridization gap and enhanced charge sensitivity. Thus, to maximize the hybridization gap, we can increase E_C^ϕ while simultaneously decreasing E_C^θ to compensate for the increased charge sensitivity. This also shows that realizing high E_C^ϕ values is critical and highly beneficial for the soft 0–π qubit, as this increases the hybridization gap with a relatively minor impact on the charge dispersion.

Next we focus on the effect of the potential energy landscape determined by the inductive energy E_L and the Josephson energy E_J on the noise sensitivity of the qubit. Figures 14(a) and 14(b) show the hybridization gap as a function of E_L and E_J for various values of the kinetic energies E_C^θ and E_C^ϕ. These results demonstrate that lowering E_J, or increasing E_L, leads to a larger hybridization gap. However, lowering E_J (or increasing E_L) also leads to a larger charge dispersion, as shown in Figs. 14(d) and 14(e). Therefore, an optimal choice for the values of E_J and E_L balances these two competing requirements. The reason why E_L also affects the tunneling in different directions (in addition to E_J, which determines the amplitude of the sinusoidal modulation in the potential) is because the minima of the potential energy of the 0 and π valleys differ by approximately $E_L\pi^2$, and thus increasing E_L leads to a smaller energy barrier between such minima. To estimate the tunneling amplitude between these minimia, we postulate an effective potential barrier of the form $V_{\text{eff}}^\theta = 2E_J - \gamma E_L$ ($V_{\text{eff}}^\phi = 2E_J - \beta E_L$) along the θ (ϕ) direction. We moreover assume that the tunneling amplitudes are given by $t_{01} \sim e^{-\alpha_\theta\sqrt{V_{\text{eff}}^\theta/E_C^\theta}}$ (at a fixed E_C^ϕ value) and $\Delta_H \sim$
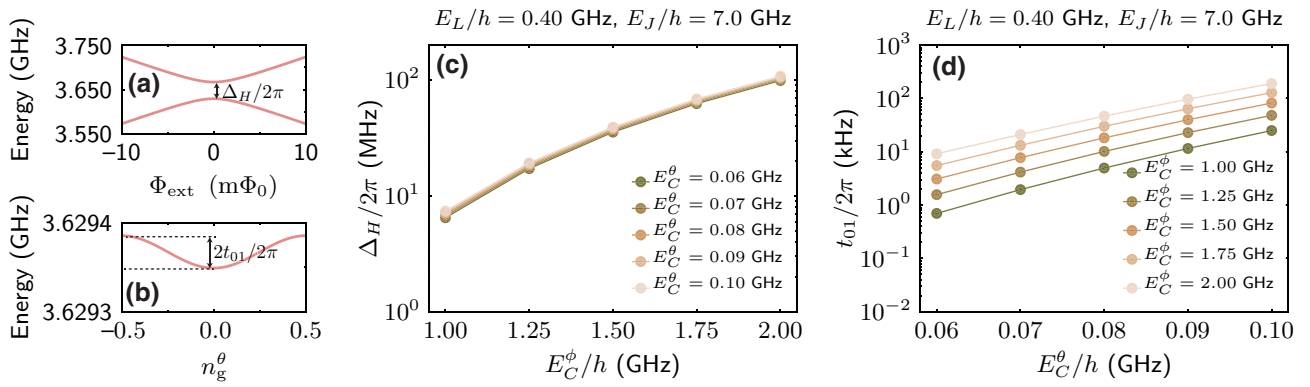
FIG. 13. (a) The hybridization gap Δ_H formed by the two lowest-lying symmetric and antisymmetric states of the π valley in the vicinity of zero external flux ($E_L/h = 0.4$ GHz, $E_J/h = 7.0$ GHz, $E_C^\phi/h = 1.5$ GHz, $E_C^\theta/h = 0.08$ GHz, $n_g^\theta = 0$). (b) The charge dispersion of the logical qubit transition energy at $\Phi_{\text{ext}} = 0$ [same device parameters as in (a)]. (c) The size of the hybridization gap and (d) the amplitude of the charge dispersion as a function of the kinetic energies. We find that Δ_H is mostly affected by E_C^ϕ, while both E_C^ϕ and E_C^θ influence t_{01}, indicating that tunneling relevant to the charge dispersion happens along an angle compared with the θ and ϕ axes.

$e^{-\alpha_\phi \sqrt{V_{\text{eff}}^\phi / E_C^\phi}}$. Remarkably, we find that this simple model accurately describes the effective potential and tunneling amplitudes in the qubit [Figs. 14(c) and 14(f)].

Finally, we must also take into account the fact that the energy of the ζ mode depends on E_L and E_C^ζ, as $E_\zeta = \sqrt{16 E_C^\zeta E_L}$. This observation favors the use of larger E_C^θ and E_L values in order to decrease the effects of photon shot noise.

The results of this section show that optimizing the performance of the soft 0–π qubit requires us to find a set
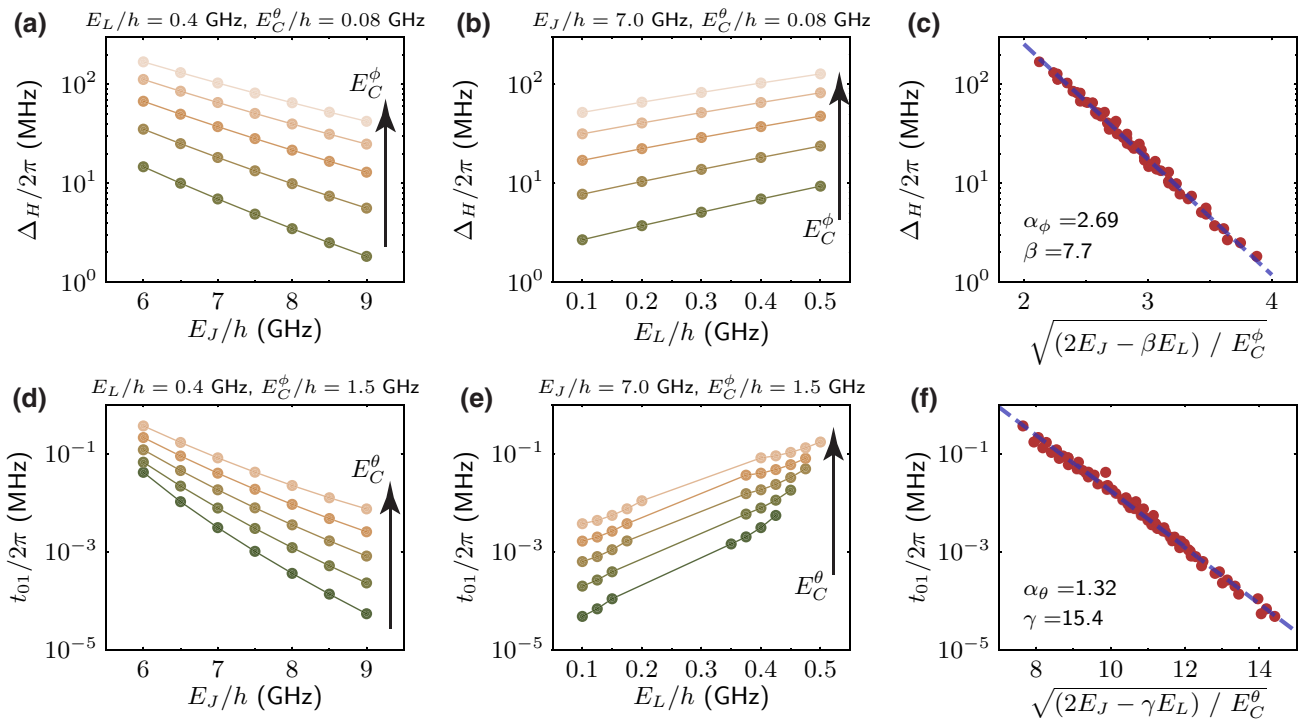

FIG. 14. (a),(b) The hybridization gap and (d),(e) charge dispersion as a function of E_J and E_L. (c),(f) the scaling of these quantities with the kinetic and potential energies. In (a) and (b), E_C^ϕ goes linearly between 1 and 2 GHz, while in (d) and (e) E_C^θ is between 0.06 and 0.10 GHz.

of parameters that balances the charge and flux sensitivity of the device. Importantly, changing certain parameters to reach the originally proposed, "deep" 0–π regime (such as lowering E_L) could, in some cases, degrade the performance of the qubit [18]. We thus find that optimizing the hybridization gap and the amplitude of the charge dispersion in the current moderate (or "soft") regime, with knowledge of the actual noise spectral density of the environment, is the most beneficial short-term direction for the soft 0–π qubit. In the longer run, however, cooling of the ζ mode and realizing highly anisotropic capacitors can enable us to reach larger degree of simultaneous charge and flux insensitivity while photon-shot-noise dephasing is also minimized.

APPENDIX F: THEORETICAL ESTIMATION OF THE DEVICE COHERENCE AND RELAXATION TIMES

With the purpose of providing theoretical upper bounds for the coherence of the device, we now present an estimation of the coherence times in the soft 0–π regime using the theory developed in Ref. [18]. The estimation is done with noise parameters that have been previously reported in the literature (see, e.g., Ref. [26]).

As argued above, thermal photon-number fluctuations of the ζ mode can lead to dephasing of the qubit states. To quantify this, we first need to determine how the ζ mode couples to the qubit modes. This coupling arises due to circuit-element disorder and the asymmetric coupling capacitance matrix of the circuit, which is shown in Fig. 10. Since we wish to capture spurious capacitive coupling to the ζ mode, the spectrum fit needs to be extended to account for the full capacitance matrix. We do this by considering each element of the circuit's capacitance matrix as a fitting parameter, while initializing the fit routine with finite-element estimations of these capacitances. This fit results in an estimate for the capacitive-coupling parameter $g_{\phi\zeta}$ ($g_{\theta\zeta}$) between the ϕ (θ) and ζ modes, which enters in the circuit Hamiltonian as an additional term of the form $\hbar g_{\phi\zeta} n_\phi n_\zeta$ ($\hbar g_{\theta\zeta} n_\theta n_\zeta$). From this extended fit we find that $g_{\phi\zeta}/2\pi \simeq 100$ MHz and $g_{\theta\zeta}/2\pi \simeq 4$ MHz, revealing that the spurious capacitive coupling is relatively strong due to the highly asymmetric coupling capacitances of the device. However, as a consequence of the large detuning between the qubit transitions and the ζ mode and the exponentially reduced transition matrix elements of the charge operators n_ϕ and n_θ, the dispersive shift of the qubit transition—due to coupling to ζ—does not exceed 2 kHz in all cases.

In addition to spurious capacitive coupling, the ζ mode couples to the qubit due to disorder in the superinductances. Assuming a conservative deviation of 10% in the area of each Josephson junction that forms the superinductors (with $N = 199$ Josephson junctions building up the superinductors), we derive [18] a coupling Hamiltonian of
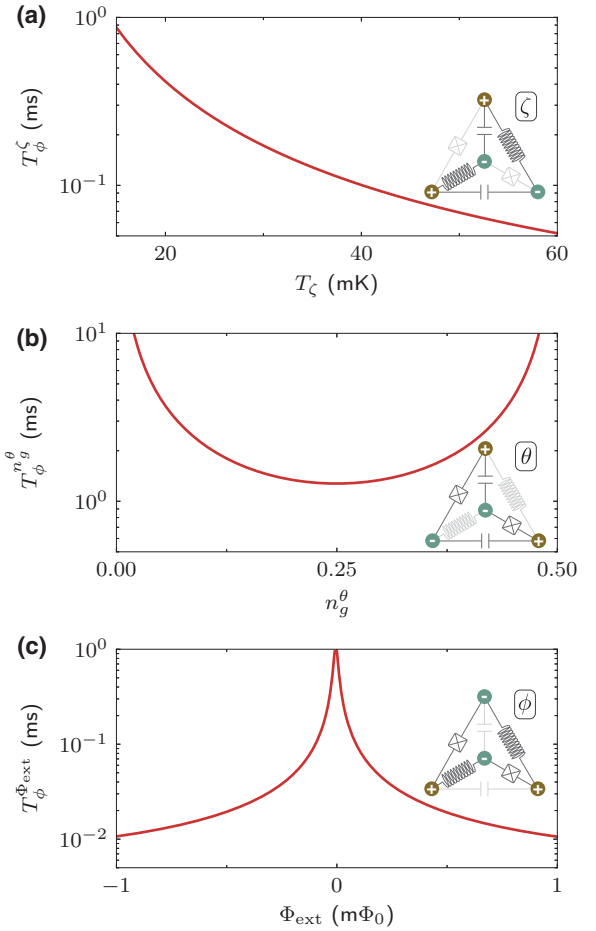

FIG. 15. Estimation of the pure-dephasing times for our qubit due to (a) photon shot noise, (b) charge noise, and (c) flux noise based on the theory in Ref. [18]. The insets shows the corresponding modes of the circuit.

the form $dE_L E_L \phi \zeta$, where $dE_L \simeq 10\%/\sqrt{N} \simeq 0.7\%$. This spurious inductive coupling also contributes to the total dispersive shift of the qubit transition, which we find to range between 1 and 10 kHz. The strength of the dispersive coupling between the qubit and the ζ mode determines the photon-shot-noise coherence time of the device [18], which is shown in Fig. 15(a) as a function of the ζ-mode temperature for $n_g = 0.25$ and $\Phi_{\text{ext}} = 0$. Although our measurements are performed at mixing chamber temperature $T_{\text{MXC}} \approx 10$ mK, following previous studies [58] we assume a ζ-mode equilibrium temperature $T_\zeta \approx 40$ mK. On the basis of these assumptions, we observe that the predicted pure-dephasing coherence time due to the coupling to the ζ mode is approximately 100 μs, which is strongly dependent on a purely theoretical and indirect estimation of the qubit–ζ-mode dispersive shift. Further experimental characterization of this dispersive shift will enable a greater understanding of ζ-mode-induced decoherence.

To complement these estimations, we also compute the pure-dephasing coherence times associated with charge noise and flux noise. Again, this is done following the theory in Ref. [18], which considers the effect of both first-order and second-order fluctuations of the noise parameters. In particular, we assume a $1/f$ spectral density for both charge noise and flux noise, with amplitudes $A_e = 10^{-4}e$ and $A_\Phi = 10^{-6}\Phi_0$ and an infrared (ultraviolet) cut-off of 1 Hz (3 GHz) [18,26]. The results are shown in Figs. 15(b) and 15(c) for charge noise and flux noise, respectively.

We notice that the experimentally measured coherence times are lower than our theoretical estimations. While this discrepancy could be partially explained by the choice of noise parameters, we hypothesize that other noise processes might also be playing a role. For instance, the occupation of the ancillary level during the Raman pulses used for qubit operation, the residual population of the readout resonator with off-resonant photons from the strong qubit-control pulses, and flux noise with white spectral density could have an impact on dephasing. While a full characterization of these noise sources is beyond of the scope of the present work and will be addressed in the future, we anticipate that further iterations of the soft 0–π design targeting the cooling of the ζ mode [19] and the implementation of faster gate schemes, enabled, for instance, by parametric modulation of the external flux, could help to mitigate these unwanted effects.

Regarding the relaxation times, we use Fermi's golden rule to estimate the lifetime of the qubit. In our model, we assume that the major limiting factor for the lifetime is the dielectric loss due to the interdigitated capacitors that substantially increase the dielectric participation ratio of the surface [59]. As discussed in the main text, such a design is necessary to realize the heavy θ mode while reducing the parasitic capacitance values that add to the mass of the ϕ mode. Since the ϕ mode does not couple to the large capacitors [Fig. 1(b)], we assume that dielectric loss affects only the θ mode. We recall that the relaxation rate from the initial state $|i\rangle$ to the final state $|f\rangle$ can be expressed as

$$\Gamma_{i \to j} = \frac{1}{\hbar^2}|\langle i|2en_\theta|j\rangle|^2 S_{VV}(\omega_{ij}), \tag{F1}$$

where the noise spectral density $S_{VV}(\omega_{ij})$ is a function of the loss tangent of the capacitor, $\tan\delta_C$, such that

$$S_{VV}(\omega) = \hbar\frac{\tan\delta_C}{C^\theta}\left(1 + \coth\frac{\hbar\omega}{2k_BT}\right). \tag{F2}$$

Equivalently, we can express this rate as a function of the qubit parameters, arriving at

$$\Gamma_{i \to j}/2\pi = |\langle i|n_\theta|j\rangle|^2 \left(\frac{8E_C^\theta}{h}\right)\tan\delta_C\left(1 + \coth\frac{\hbar\omega}{2k_BT}\right). \tag{F3}$$

Since the first plasmon transition in our qubit is below the logical qubit energy, there are two paths for the qubit to decay: directly to the ground state $|\pi_s^+\rangle \to |0_s\rangle$, or through the first plasmon state $|\pi_s^+\rangle \to |0_{p\theta}\rangle \to |0_s\rangle$. Since the plasmon transition $|0_{p\theta}\rangle \to |0_s\rangle$ is not protected (we measure $T_1^{\text{plasmon}} = 1.8~\mu\text{s}$), the two main contributions to the decay are the transitions to the ground state and to the first plasmon state. Thus, we can write at low temperatures

$$1/T_1 \approx \left\{|\langle\pi_s^+|n_\theta|0_s\rangle|^2 + |\langle\pi_s^+|n_\theta|0_{p\theta}\rangle|^2\right\}$$
$$\times \left(16E_C^\theta/h\right)\tan\delta_C. \tag{F4}$$

Because the fluxon transition matrix elements are much smaller than those of the plasmon transition (e.g., $\langle\pi_s^+|n_\theta|0_s\rangle \approx \langle 0_{p\theta}|n_\theta|0_s\rangle/200$ and $\langle\pi_s^+|n_\theta|0_{p\theta}\rangle \approx \langle 0_{p\theta}|n_\theta|0_s\rangle/50$), this simple model suggests a 3 orders of magnitude increase of the logical T_1 with respect to that of the plasmon transition. Indeed, our measurements of $T_1^{\text{plasmon}} = 1.8~\mu\text{s}$ and $T_1 = 1.6$ ms reflect very well this fact and yield a dielectric loss tangent of $\tan\delta_C \approx 5 \times 10^{-4}$.

APPENDIX G: TWO-TONE RAMAN PULSE SCHEME

We model the Raman pulse scheme in the qubit by truncating the energy-level structure to the ground states of the valleys $|0_s\rangle$, $|\pi_s^+\rangle$ and the intermediate level $|\pi_{d\theta}^-\rangle$. For simplicity, we relabel these levels by $|0_s\rangle \to |0\rangle$, $|\pi_s^+\rangle \to |2\rangle$, and $|\pi_{d\theta}^-\rangle \to |1\rangle$ [see Fig. 16(a)]. We first consider the unitary evolution of this Λ system driven by two classical fields: [42]

$$H/\hbar = \omega_1\sigma_{11} + \omega_2\sigma_{22} + [\Omega_\alpha\cos(\omega_\alpha t)\sigma_{01}$$
$$+ \Omega_\beta\cos(\omega_\beta t)\sigma_{12} + \text{h.c.}], \tag{G1}$$

where $\omega_0 = 0 < \omega_2 < \omega_1$ are the eigenenergies of $|0\rangle$, $|2\rangle$, and $|1\rangle$, respectively, ω_α and ω_β are the frequencies of the drive tones with amplitudes Ω_α and Ω_β, respectively, and $\sigma_{ij} = |i\rangle\langle j|$ for $i,j \in [1,2,3]$. We moreover assume that the α (β) drive addresses only the $|0\rangle \leftrightarrow |1\rangle$ ($|1\rangle \leftrightarrow |2\rangle$) transition.

Moving to a rotating frame where the drives are equally detuned from the ancillary level $|1\rangle$ (i.e., $\omega_\alpha = \omega_1 - \Delta$, $\omega_\beta = \omega_1 - \omega_2 - \Delta$) and performing the rotating wave approximation, we find Eq. (G1) takes the time-independent form of

$$\tilde{H}/\hbar = \Delta\sigma_{11} + \left(\frac{1}{2}\Omega_\alpha\sigma_{01} + \frac{1}{2}\Omega_\beta\sigma_{12} + \text{h.c.}\right). \tag{G2}$$
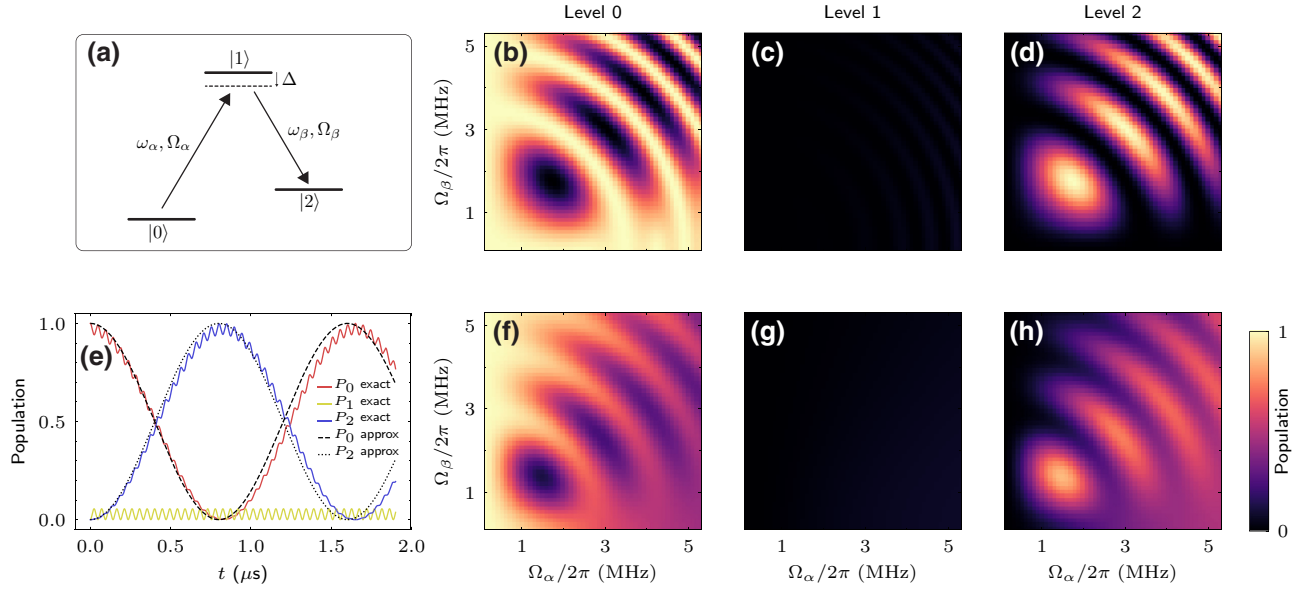
FIG. 16.   (a) Three soft 0–π qubit levels coupled to two microwave drives forming a Λ system. (b)–(d) Level population as a function of the drive amplitudes based on the analytical results of the time evolution of the system ($t = 6.7$ μs, $\Delta/2\pi = 20$ MHz). (e) Level population as a function of time based on the exact results for the effective two-level system ($\Omega_\alpha/2\pi = \Omega_\beta/2\pi = 5$ MHz, $\Delta/2\pi = 20$ MHz). (f)–(h) Results of the numerical simulation for two Gaussian pulses with $\sigma = 1$ μs, $\Delta/2\pi = 3$ MHz, relaxation rates $\Gamma_{10}/2\pi = \Gamma_{12}/2\pi = 100$ kHz, and dephasing rate $\Gamma_1^\phi/2\pi = 500$ kHz.

Defining $\tilde\Omega = \sqrt{\Delta^2 + \Omega_\alpha^2 + \Omega_\beta^2}$, we find the eigenfrequencies of Eq. (G2) are given by

$$\epsilon_0 = 0,$$
$$\epsilon_\pm = \frac{1}{2}\left(\Delta \pm \tilde\Omega\right), \qquad (G3)$$

and correspond to the dressed states

$$|\Psi_0\rangle = -\Omega_\beta|0\rangle + \Omega_\alpha|2\rangle,$$
$$|\Psi_\pm\rangle = \Omega_\alpha|0\rangle + (\Delta \pm \tilde\Omega)|1\rangle + \Omega_\beta|2\rangle, \qquad (G4)$$

respectively.

For analytical calculations, we assume that the system at $t = 0$ is initialized in the $|0\rangle$ state when the drives are instantaneously turned on (square pulse). The time evolution of the system can be obtained by transformation to the dressed basis, where the system evolves to the state $|\Psi(t)\rangle = \alpha(t)|0\rangle + \beta(t)|1\rangle + \gamma(t)|2\rangle$ at time t, where

$$\alpha(t) = \frac{\Omega_\alpha^2}{\Omega_\alpha^2 + \Omega_\beta^2} \times \left[\frac{\Omega_\beta^2}{\Omega_\alpha^2} + e^{-i\Delta t/2}\right.$$

$$\left.\times \left(\cos\frac{\tilde\Omega t}{2} + i\frac{\Delta}{\tilde\Omega}\sin\frac{\tilde\Omega t}{2}\right)\right], \qquad (G5)$$

$$\beta(t) = \frac{\Omega_\alpha}{\tilde\Omega} \times \left(-ie^{-i\Delta t/2}\sin\frac{\tilde\Omega t}{2}\right), \qquad (G6)$$

$$\gamma(t) = \frac{\Omega_\alpha\Omega_\beta}{\Omega_\alpha^2 + \Omega_\beta^2} \times \left[-1 + e^{-i\Delta t/2}\right.$$

$$\left.\times \left(\cos\frac{\tilde\Omega t}{2} + i\frac{\Delta}{\tilde\Omega}\sin\frac{\tilde\Omega t}{2}\right)\right]. \qquad (G7)$$

Figure 16(e) shows the level populations as a function of time for $\Omega_1 = \Omega_2$. We observe Rabi oscillations between the two lowest-lying states, $|0\rangle$ and $|2\rangle$, with only a negligible population in the intermediate level, $|1\rangle$. Interestingly, the Rabi oscillation features a superimposed low-amplitude, high-frequency modulation [42]. Adiabatic elimination of the intermediate level in the vicinity of equal drives $\Omega_1 \approx \Omega_2$ leads to an effective two-level system [43] with a Rabi rate of $\Omega_R = \Omega_1\Omega_2/2\Delta$. This effective model is in good agreement with the exact analytical solution [dashed and dotted lines in Fig. 16(e)].

Figures 16(b)–16(d) show the level population at a given time as a function of the drive amplitude and detuning, similar to the pulsed measurements performed in our experiment. The results show that maximal population transfer between $|0\rangle$ and $|2\rangle$ is possible when the drives are equal.

In addition to the analytical estimations, we perform numerical simulations using the QuTiP software package [60] to solve the time evolution of the system involving Gaussian-shaped pulses and decay mechanisms using a Lindblad master equation solver. The result of the numerical simulation is in very good agreement with our experimental findings [Figs. 5(c) and 16(f)–16(h)].

[1] M. A. Nielsen and I. L. Chuang, *Quantum Computation and Quantum Information* (Cambridge University Press, NY, 2011).

[2] M. H. Devoret and R. J. Schoelkopf, Superconducting circuits for quantum information: An outlook, Science **339**, 1169 (2013).

[3] E. Knill, Quantum computing with realistically noisy devices, Nature **434**, 39 (2005).

[4] P. W. Shor, Scheme for reducing decoherence in quantum computer memory, Phys. Rev. A **52**, R2493 (1995).

[5] M. D. Reed, L. DiCarlo, S. E. Nigg, L. Sun, L. Frunzio, S. M. Girvin, and R. J. Schoelkopf, Realization of three-qubit quantum error correction with superconducting circuits, Nature **482**, 382 (2012).

[6] J. Kelly, R. Barends, A. G. Fowler, A. Megrant, E. Jeffrey, T. C. White, D. Sank, J. Y. Mutus, B. Campbell, Y. Chen, Z. Chen, B. Chiaro, A. Dunsworth, I.-C. Hoi, C. Neill, P. J. J. O'Malley, C. Quintana, P. Roushan, A. Vainsencher, J. Wenner, A. N. Cleland, and J. M. Martinis, State preservation by repetitive error detection in a superconducting quantum circuit, Nature **519**, 66 (2015).

[7] N. Ofek, A. Petrenko, R. Heeres, P. Reinhold, Z. Leghtas, B. Vlastakis, Y. Liu, L. Frunzio, S. M. Girvin, L. Jiang, M. Mirrahimi, M. H. Devoret, and R. J. Schoelkopf, Extending the lifetime of a quantum bit with error correction in superconducting circuits, Nature **536**, 441 (2016).

[8] L. B. Ioffe, M. V. Feigel'man, A. Ioselevich, D. Ivanov, M. Troyer, and G. Blatter, Topologically protected quantum bits using Josephson junction arrays, Nature **415**, 503 (2002).

[9] B. Douçot, M. V. Feigel'man, and L. B. Ioffe, Topological Order in the Insulating Josephson Junction Array, Phys. Rev. Lett. **90**, 107003 (2003).

[10] A. Kitaev, Fault-tolerant quantum computation by anyons, Ann. Phys. **303**, 2 (2003).

[11] A. Kitaev, arXiv:cond-mat/0609441v2 (2006).

[12] P. Brooks, A. Kitaev, and J. Preskill, Protected gates for superconducting qubits, Phys. Rev. A **87**, 052306 (2013).

[13] D. Gottesman, A. Kitaev, and J. Preskill, Encoding a qubit in an oscillator, Phys. Rev. A **64**, 012310 (2001).

[14] B. Douçot and L. B. Ioffe, Physical implementation of protected qubits, Rep. Prog. Phys. **75**, 072001 (2012).

[15] S. Gladchenko, D. Olaya, E. Dupont-Ferrier, B. Douçot, L. B. Ioffe, and M. E. Gershenson, Superconducting nanocircuits for topologically protected qubits, Nat. Phys. **5**, 48 (2008).

[16] M. T. Bell, J. Paramanandam, L. B. Ioffe, and M. E. Gershenson, Protected Josephson Rhombus Chains, Phys. Rev. Lett. **112**, 167001 (2014).

[17] J. M. Dempster, B. Fu, D. G. Ferguson, D. I. Schuster, and J. Koch, Understanding degenerate ground states of a protected quantum circuit in the presence of disorder, Phys. Rev. B **90**, 094518 (2014).

[18] P. Groszkowski, A. D. Paolo, A. L. Grimsmo, A. Blais, D. I. Schuster, A. A. Houck, and J. Koch, Coherence properties of the $0 - \pi$ qubit, New J. Phys. **20**, 043053 (2018).

[19] A. D. Paolo, A. L. Grimsmo, P. Groszkowski, J. Koch, and A. Blais, Control and coherence time enhancement of the $0 - \pi$ qubit, New J. Phys. **21**, 043002 (2019).

[20] W. C. Smith, A. Kou, X. Xiao, U. Vool, and M. H. Devoret, Superconducting circuit protected by two-Cooper-pair tunneling, npj Quantum Inf. **6**, 8 (2020).

[21] K. Kalashnikov, W. T. Hsieh, W. Zhang, W.-S. Lu, P. Kamenov, A. Di Paolo, A. Blais, M. E. Gershenson, and M. Bell, Bifluxon: Fluxon-parity-protected superconducting qubit, PRX Quantum **1**, 010307 (2020).

[22] A. Fedorov, P. Macha, A. K. Feofanov, C. J. P. M. Harmans, and J. E. Mooij, Tuned Transition from Quantum to Classical for Macroscopic Quantum States, Phys. Rev. Lett. **106**, 170404 (2011).

[23] N. Earnest, S. Chakram, Y. Lu, N. Irons, R. K. Naik, N. Leung, L. Ocola, D. A. Czaplewski, B. Baker, J. Lawrence, J. Koch, and D. I. Schuster, Realization of a Λ System with Metastable States of a Capacitively Shunted Fluxonium, Phys. Rev. Lett. **120**, 150504 (2018).

[24] Y.-H. Lin, L. B. Nguyen, N. Grabon, J. San Miguel, N. Pankratova, and V. E. Manucharyan, Demonstration of Protection of a Superconducting Qubit from Energy Decay, Phys. Rev. Lett. **120**, 150503 (2018).

[25] P. Campagne-Ibarcq, A. Eickbusch, S. Touzard, E. Zalys-Geller, N. E. Frattini, V. V. Sivak, P. Reinhold, S. Puri, S. Shankar, R. J. Schoelkopf, L. Frunzio, M. Mirrahimi, and M. H. Devoret, Quantum error correction of a qubit encoded in grid states of an oscillator, Nature **584**, 368 (2020).

[26] J. Koch, T. M. Yu, J. Gambetta, A. A. Houck, D. I. Schuster, J. Majer, A. Blais, M. H. Devoret, S. M. Girvin, and R. J. Schoelkopf, Charge-insensitive qubit design derived from the Cooper pair box, Phys. Rev. A **76**, 042319 (2007).

[27] I. V. Pechenezhskiy, R. A. Mencia, L. B. Nguyen, Y.-H. Lin, and V. E. Manucharyan, The superconducting quasicharge qubit, Nature **585**, 368 (2020).

[28] J. Gambetta, A. Blais, D. I. Schuster, A. Wallraff, L. Frunzio, J. Majer, M. H. Devoret, S. M. Girvin, and R. J. Schoelkopf, Qubit-photon interactions in a cavity: Measurement-induced dephasing and number splitting, Phys. Rev. A **74**, 042318 (2006).

[29] U. Vool and M. Devoret, Introduction to quantum electromagnetic circuits, Int. J. Circ. Theor. Appl. **45**, 897 (2017).

[30] V. E. Manucharyan, J. Koch, L. I. Glazman, and M. H. Devoret, Fluxonium: Single cooper-pair circuit free of charge offsets, Science **326**, 113 (2009).

[31] S. Krastanov, V. V. Albert, C. Shen, C.-L. Zou, R. W. Heeres, B. Vlastakis, R. J. Schoelkopf, and L. Jiang, Universal control of an oscillator with dispersive coupling to a qubit, Phys. Rev. A **92**, 040303 (2015).

[32] A. Wallraff, D. I. Schuster, A. Blais, L. Frunzio, R.-S. Huang, J. Majer, S. Kumar, S. M. Girvin, and R. J.

Schoelkopf, Strong coupling of a single photon to a superconducting qubit using circuit quantum electrodynamics, Nature **431**, 162 (2004).

[33] A. Blais, R.-S. Huang, A. Wallraff, S. M. Girvin, and R. J. Schoelkopf, Cavity quantum electrodynamics for superconducting electrical circuits: An architecture for quantum computation, Phys. Rev. A **69**, 062320 (2004).

[34] J. Aumentado, M. W. Keller, J. M. Martinis, and M. H. Devoret, Nonequilibrium Quasiparticles and 2*e* Periodicity in Single-Cooper-Pair Transistors, Phys. Rev. Lett. **92**, 066802 (2004).

[35] J. A. Schreier, A. A. Houck, J. Koch, D. I. Schuster, B. R. Johnson, J. M. Chow, J. M. Gambetta, J. Majer, L. Frunzio, M. H. Devoret, S. M. Girvin, and R. J. Schoelkopf, Suppressing charge noise decoherence in superconducting charge qubits, Phys. Rev. B **77**, 180502 (2008).

[36] L. Sun, L. DiCarlo, M. D. Reed, G. Catelani, L. S. Bishop, D. I. Schuster, B. R. Johnson, G. A. Yang, L. Frunzio, L. Glazman, M. H. Devoret, and R. J. Schoelkopf, Measurements of Quasiparticle Tunneling Dynamics in a Band-Gap-Engineered Transmon Qubit, Phys. Rev. Lett. **108**, 230509 (2012).

[37] D. Ristè, C. C. Bultink, M. J. Tiggelman, R. N. Schouten, K. W. Lehnert, and L. DiCarlo, Millisecond charge-parity fluctuations and induced decoherence in a superconducting transmon qubit, Nat. Commun. **4**, 1913 EP (2013).

[38] K. Serniak, M. Hays, G. de Lange, S. Diamond, S. Shankar, L. D. Burkhart, L. Frunzio, M. Houzet, and M. H. Devoret, Hot Nonequilibrium Quasiparticles in Transmon Qubits, Phys. Rev. Lett. **121**, 157701 (2018).

[39] M. Baur, S. Filipp, R. Bianchetti, J. M. Fink, M. Göppl, L. Steffen, P. J. Leek, A. Blais, and A. Wallraff, Measurement of Autler-Townes and Mollow Transitions in a Strongly Driven Superconducting Qubit, Phys. Rev. Lett. **102**, 243602 (2009).

[40] M. A. Sillanpää, J. Li, K. Cicak, F. Altomare, J. I. Park, R. W. Simmonds, G. S. Paraoanu, and P. J. Hakonen, Autler-Townes Effect in a Superconducting Three-Level System, Phys. Rev. Lett. **103**, 193601 (2009).

[41] S. Novikov, J. E. Robinson, Z. K. Keane, B. Suri, F. C. Wellstood, and B. S. Palmer, Autler-townes splitting in a three-dimensional transmon superconducting qubit, Phys. Rev. B **88**, 060503 (2013).

[42] G. Chimczak and R. Tanaś, Fine tuning of quantum operations performed via Raman transitions, Phys. Rev. A **77**, 032312 (2008).

[43] D. A. Steck, Quantum and Atom Optics (available online at http://steck.us/teaching, 2017).

[44] A. P. M. Place, L. V. H. Rodgers, P. Mundada, B. M. Smitham, M. Fitzpatrick, Z. Leng, A. Premkumar, J. Bryon, S. Sussman, G. Cheng, T. Madhavan, H. K. Babla, B. Jaeck, A. Gyenis, N. Yao, R. J. Cava, N. P. de Leon, and A. A. Houck, arXiv:2003.00024 [quant-ph] (2020).

[45] L. B. Nguyen, Y.-H. Lin, A. Somoroff, R. Mencia, N. Grabon, and V. E. Manucharyan, High-Coherence Fluxonium Qubit, Phys. Rev. X **9**, 041041 (2019).

[46] R. Zhao, S. Park, T. Zhao, M. Bal, C. R. H. McRae, J. Long, and D. P. Pappas, Merged-Element Transmon, Phys. Rev. Appl. **14**, 064006 (2020).

[47] N. A. Masluk, I. M. Pop, A. Kamal, Z. K. Minev, and M. H. Devoret, Microwave Characterization of Josephson Junction Arrays: Implementing a Low Loss Superinductance, Phys. Rev. Lett. **109**, 137002 (2012).

[48] T. Hazard, A. Gyenis, A. Di Paolo, A. Asfaw, S. A. Lyon, A. Blais, and A. A. Houck, Nanowire Superinductance Fluxonium Qubit, Phys. Rev. Lett. **122**, 010504 (2019).

[49] H. Zhang, S. Chakram, T. Roy, N. Earnest, Y. Lu, Z. Huang, D. Weiss, J. Koch, and D. I. Schuster, Universal Fast-Flux Control of a Coherent, Low-Frequency Qubit, Phys. Rev. X **11**, 011010 (2021).

[50] M. Abdelhafez, B. Baker, A. Gyenis, P. Mundada, A. A. Houck, D. Schuster, and J. Koch, Universal gates for protected superconducting qubits using optimal control, Phys. Rev. A **101**, 022321 (2020).

[51] J. M. Chow, J. M. Gambetta, A. W. Cross, S. T. Merkel, C. Rigetti, and M. Steffen, Microwave-activated conditional-phase gate for superconducting qubits, New J. Phys. **15**, 115012 (2013).

[52] K. N. Nesterov, I. V. Pechenezhskiy, C. Wang, V. E. Manucharyan, and M. G. Vavilov, Microwave-activated controlled-*z* gate for fixed-frequency fluxonium qubits, Phys. Rev. A **98**, 030301 (2018).

[53] S. Puri, A. Grimm, P. Campagne-Ibarcq, A. Eickbusch, K. Noh, G. Roberts, L. Jiang, M. Mirrahimi, M. H. Devoret, and S. M. Girvin, Stabilized cat in a Driven Nonlinear Cavity: A Fault-Tolerant Error Syndrome Detector, Phys. Rev. X **9**, 041009 (2019).

[54] J. Guillaud and M. Mirrahimi, Repetition cat Qubits for Fault-Tolerant Quantum Computation, Phys. Rev. X **9**, 041053 (2019).

[55] V. Fatemi, A. R. Akhmerov, and L. Bretheau, arXiv:2008.13758 [cond-mat.mes-hall] (2020).

[56] M. T. Bell, W. Zhang, L. B. Ioffe, and M. E. Gershenson, Spectroscopic Evidence of the Aharonov-Casher Effect in a Cooper Pair box, Phys. Rev. Lett. **116**, 107002 (2016).

[57] A. Wallraff, D. I. Schuster, A. Blais, J. M. Gambetta, J. Schreier, L. Frunzio, M. H. Devoret, S. M. Girvin, and R. J. Schoelkopf, Sideband Transitions and Two-Tone Spectroscopy of a Superconducting Qubit Strongly Coupled to an On-Chip Cavity, Phys. Rev. Lett. **99**, 050501 (2007).

[58] Z. Wang, S. Shankar, Z. Minev, P. Campagne-Ibarcq, A. Narla, and M. Devoret, Cavity Attenuators for Superconducting Qubits, Phys. Rev. Appl. **11**, 014031 (2019).

[59] C. Wang, C. Axline, Y. Y. Gao, T. Brecht, Y. Chu, L. Frunzio, M. H. Devoret, and R. J. Schoelkopf, Surface participation and dielectric loss in superconducting qubits, Appl. Phys. Lett. **107**, 162601 (2015).

[60] J. Johansson, P. Nation, and F. Nori, Qutip: An open-source python framework for the dynamics of open quantum systems, Comput. Phys. Commun. **183**, 1760 (2012).